

# Location and probability of shoal margin collapses in a sandy estuary

Wout M. van Dijk,<sup>1\*</sup> Dick R. Mastbergen,<sup>2</sup> Geeralt A. van den Ham,<sup>3</sup> Jasper R. F. W. Leuven<sup>1</sup> and Maarten G. Kleinhans<sup>1</sup>

<sup>1</sup> Department of Physical Geography, Faculty of Geosciences, Utrecht University, Utrecht, The Netherlands

<sup>2</sup> Department of Ecosystems and Sediment Dynamics, Deltares, Delft, The Netherlands

<sup>3</sup> Department of Geo-engineering, Deltares, Delft, The Netherlands

Received 31 May 2017; Revised 19 March 2018; Accepted 22 March 2018

\*Correspondence to: Wout M. van Dijk, Department of Physical Geography, Faculty of Geosciences, Utrecht University, Utrecht, The Netherlands. E-mail: W.M.vanDijk@uu.nl

This is an open access article under the terms of the Creative Commons Attribution License, which permits use, distribution and reproduction in any medium, provided the original work is properly cited.

ESPL

Earth Surface Processes and Landforms

**ABSTRACT:** Channel bank failure, and collapses of shoal margins and beaches due to flow slides, have been recorded in Dutch estuaries for the past 200 years but have hardly been recognized elsewhere. Current predictions lack forecasting capabilities, because they were validated and calibrated for historic data of cross-sections in specific systems, allowing local hindcast rather than location and probability forecasting. The objectives of this study were to investigate where on shoal margins collapses typically occur and what shoal margin collapse geometries and volumes are, such that we can predict their occurrence. We identified shoal margin collapses, generally completely submerged, from bathymetry data by analyzing digital elevation models of difference of the Western Scheldt for the period 1959–2015. We used the bathymetry data to determine the conditions for occurrence, specifically to obtain slope height and angle, and applied these variables in a shoal margin collapse predictor. We found 299 collapses along 300 km of shoal margin boundaries over 56 years, meaning that more than five collapses occur on average per year. The average shoal margin collapse body is well approximated by a 1/3 ellipsoid shape, covers on average an area of 34 000 m<sup>2</sup> and has an average volume of 100 000 m<sup>3</sup>. Shoal margin collapses occur mainly at locations where shoals take up a proportionally larger area than average in the cross-section of the entire estuary, and occur most frequently where lateral shoal margin displacement is low. A receiver operating characteristic curve shows that the forecasting method predicts the shoal margin collapse location well. We conclude that the locations of the shoal margin collapses are well predicted by the variation in conditions of the relative slope height and angle within the Western Scheldt, and likely locations are at laterally relatively stable shoal margins. This provides hypotheses aiding the recognition of these features in sandy estuaries worldwide. Copyright © 2018 John Wiley & Sons, Ltd.

**KEYWORDS:** shoal margin collapse; flow slide; shoal morphodynamics; Western Scheldt; forecasting tool; estuaries

## Introduction

Channel bank failure, and collapses of shoal margins and beaches due to flow slides, have been recognized in estuaries and rivers around the world (Coleman, 1969; Laury, 1971; Silvis and De Groot, 1995; Torrey 1995; Dunbar *et al.*, 1999; Van den Berg *et al.*, 2002, 2017; Beinssen *et al.*, 2014; Beinssen and Mastbergen, 2017). ‘Channel banks’ refer to the estuary margins, which in the Western Scheldt at present are protected from erosion. Shoals and tidal flats are inside the estuary and are not protected against erosion. ‘Collapses’ refer to a downfall of the elevation in the morphology in a relatively short time. The style and development of failure processes are controlled by flow conditions, slope geometry and sand properties (Stoutjesdijk *et al.*, 1998; Olson and Stark, 2002; Deangeli, 2007; Van den Ham *et al.*, 2014). The morphological and societal importance of shoal margin collapses is considerable: typically, events occur up to several million cubic meters in the Western Scheldt (Figure 1) and approach annually dredged volumes of  $10 \times 10^6$  m<sup>3</sup> (Wang and Winterwerp, 2001; Dam

*et al.*, 2007; Jeuken and Wang, 2010). Moreover, collapses caused serious damage to dikes and polders and threatened the levees and stability of vital constructions such as the Eastern Scheldt storm surge barrier (Stoutjesdijk *et al.*, 2012). Deposition due to large shoal margin collapses in the Western Scheldt is sometimes a problem as the fairway requires a certain minimal depth to the harbor of Antwerp. Numerical morphodynamic models of the complete estuary have ignored channel–shoal margin collapses so far and inadequately predict gentle slope processes and mud settling. We would like to investigate the effects on large-scale dynamics of channels and shoals and explore dredging and dumping scenarios that optimize cost and benefit habitat surface area and quality. However, before including the process of shoal margin collapse into a numerical morphodynamic model, we must first understand the spatial pattern, organization and geometries of shoal margin collapses.

Two fundamentally different types of underwater shoal margin collapses occur: rapid flow slides due to liquefaction and the more dominantly slow retrogressive flow slides due to

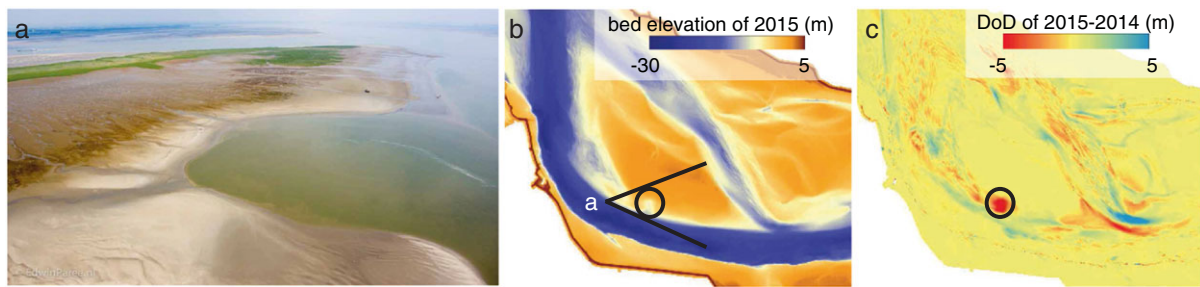


**Figure 1.** Example of a shoal margin collapse in the Western Scheldt Estuary. (a) Aerial view of the tidal flat of Walsoorden after the July 2014 collapse (photo courtesy of Edwin Pree, Rijkswaterstaat Zee en Delta, Middelburg, Netherlands). (b) Bathymetry data ('vakkloedingen') from the tidal flat of Walsoorden for 2015. (c) Example DoD between consecutive years used to identify location, geometry and shape of shoal margin collapses, here for the case shown in (a) and (b).

breaching (Van den Berg *et al.*, 2002, 2017; Van den Ham *et al.*, 2014; Mastbergen *et al.*, 2016). Flow slides occur at lower angles and displace much more sediment over much larger distances than the well-known classic (river) bank shear failure that is followed by a slump or slide over a short distance (Simon and Collinson, 2002; Kleinhans *et al.*, 2009). Besides, these shoal margin collapses often occur at the inner side of a bend, unlike the classical channel bank failure, which occurs at the outer side of a meander bend. The general failure mechanisms of channel banks proceed from undercutting by sand removal on the transverse bed slope at the bank toe. The processes of liquefaction and breaching require different conditions (see Van den Berg *et al.*, 2002; Van den Ham *et al.*, 2014). Liquefaction requires loosely packed, non-lithified and water-saturated sand or silt (Lowe, 1976), whereas breaching requires the presence of a sufficiently large body of densely packed fine sand or silt (You *et al.*, 2014; Van den Berg *et al.*, 2017). Liquefied flow slides and breaching both occur at sufficiently high and steep slopes. Before breaching can start, a steep slope can be made by dredging. Under natural conditions it can be produced by the scar of a liquefaction flow slide, especially when breaching occurs in an originally rather gently sloping inner bend, e.g. at the shoal margin (Van den Berg *et al.*, 2017).

These processes of liquefaction and breaching are included in two models as follows. The HMBreach model assesses the sensitivity of a submerged slope with given geometry and sand properties to breaching, by calculating the minimum size of the initial breach necessary to maintain the steep slope, keep the breaching process going and considerably expand the size of the failure for it to trigger a self-accelerating breach flow (Mastbergen and Van den Berg, 2003; Mastbergen 2009). The SLIQ2D model calculates whether in a submerged slope a static liquefaction might occur or not, based on the slope geometry, the relative density and the material properties of the sand or silt (Stoutjesdijk, 1994; Stoutjesdijk *et al.*, 1998). Van den Ham *et al.* (2014) argued that these theoretical liquefaction and breaching models quantify the relative influences of channel geometry and soil parameters, but the reliability of the estimated probability remains limited. Therefore, Van den Ham *et al.* (2014) proposed a semi-empirical model that predicts the probability of shoal margin collapses. This predictor includes an empirical factor based on the frequency of historical flow slides in Zeeland (Wilderom, 1979). The prediction method is extended with a sensitivity for density and sand particle size, based on the assumption that flow slides may be generated either by liquefaction or by breaching (Van den Ham *et al.*, 2014). The method of Van den Ham *et al.* (2014) is mainly applied for hindcasting, i.e. to test by observing whether it would have correctly predicted a bank collapse, and to anticipate the probability of channel bank collapses per

kilometer per year, but has not been tested on spatial elevation maps for the occurrence of shoal margin collapses.

Here we study shoal margin collapses based on bed elevation data of the Western Scheldt for the period 1959–2015. The tidal flats of the Western Scheldt, including the shoals, have increased in height and steepness over the past decades (De Vet *et al.*, 2017), leading to conditions that are favorable for new collapses and stressing the need for a predictor of locations, probabilities and dimensions. The objectives of this study were to identify spatial patterns of shoal margin collapses, determine their geometries and dimensions, modify the method of Van den Ham *et al.* (2014) to predict shoal margin collapses and assess the accuracy of this prediction with observed shoal margin collapse locations. In this paper, we first give a detailed description of the study area and describe the methods and data that are used for the spatial pattern analysis and geometries of shoal margin collapses. Then, we present the map of shoal margin collapses, shoal geometry distributions and probability of occurrence in the Western Scheldt. Finally, we modify the applied forecasting method and explore its potential implications for numerical models.

## Study Area

For reasons of data availability, this study focuses on the Western Scheldt, which is located in the southwestern part of the Netherlands and is the seaward section (60 km) of the tide-dominated Scheldt estuary. The estuary is 200 km long and stretches up to Gent in Belgium (Figure 2a). The Western Scheldt is characterized as a multiple channel system, with a well-developed system of channels and shoals. It has, on average, a trumpet-shaped geometry and covers an area of about 370 km<sup>2</sup>. The main driving force of the system is the tide. Due to land reclamation, shore protection and dredging of the navigation fairway in past centuries, the tidal range in the eastern part of the basin has increased significantly. It ranges nowadays from 3.8 m at the estuary entrance to 5 m at the Dutch/Belgian border (Van den Berg *et al.*, 1996; Jeuken, 2000). The tidal prism at the mouth is about  $2 \times 10^9$  m<sup>3</sup> (Wang *et al.*, 2002), in which the total flood discharge of a tidal cycle (flood volume) is on average  $1.1 \times 10^9$  m<sup>3</sup> at Vlissingen and reduces to  $70 \times 10^6$  m<sup>3</sup> at Antwerp (Van den Berg *et al.*, 1996), whereas the yearly-averaged river discharge of the Scheldt into the Western Scheldt is a negligible  $120$  m<sup>3</sup> s<sup>-1</sup>, causing the estuary to be well mixed (Cancino and Neves, 1999; De Vriend *et al.*, 2011). Relative fine sediment is found in the estuary: median grain size  $D_{50}$  of the channel bed varies between about 200 and 300  $\mu$ m, whereas sediment at the higher parts of the shoals is generally smaller than 200  $\mu$ m. Additionally,

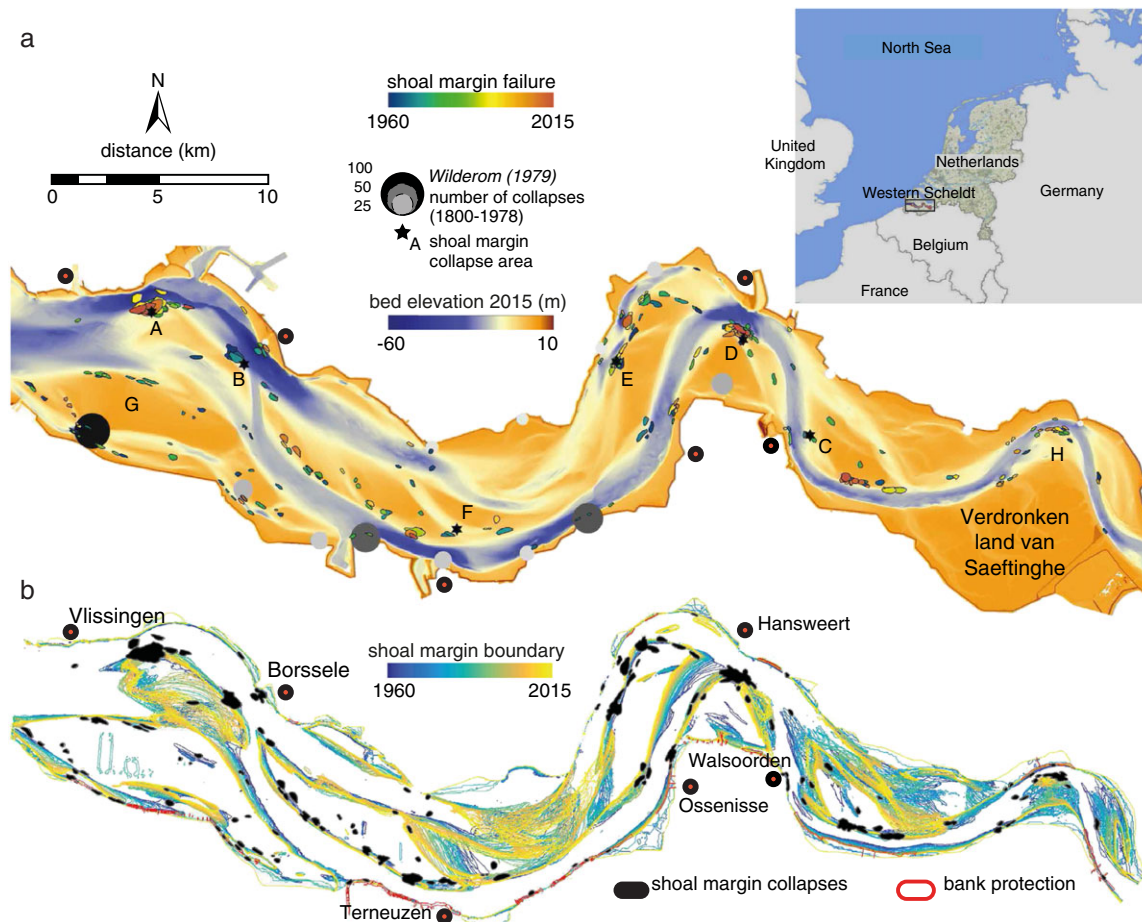


**Figure 2.** Shoal margin collapses and migration in the Western Scheldt in the period 1960–2015. (a) DEM for the Western Scheldt with dominant locations for stretches with bank and shoal margin collapses identified by Wilderom (1979), and shoal margin collapses identified in this study. Symbols a–h are the tidal flats in the Western Scheldt; the ‘Spijkerplaat’ (A) west and (B) east, (C) ‘Plaat van Walsoorden’, (D) ‘Platen van Ossensisse’, (E) ‘Middelplaat’, (F) ‘Brouwersplaat’, (G) ‘Hooge Platen’ and (H) ‘Verdronken Land van Saeftinghe’. (b) Shoal margin location at mean bed elevation per year for the period 1960–2015 illustrates that collapses occur mostly along laterally immobile shoal margin locations.

10–20% of the intertidal areas is dominantly covered by mud (Braat *et al.*, 2017).

The Western Scheldt provides access to various harbors, of which the port of Antwerp (Belgium) is the largest. Shoal margin collapses impact the fairway as sediment deposits into the channel and affects the width and depth. Channel bank failures have been recorded in the Western Scheldt and Eastern Scheldt estuary for the past 200 years. Between the 1800s and 1970s more than 448 large channel bank failures with sediment volumes up to a million cubic meters were documented in soundings of the Western Scheldt (Figure 2a, Wilderom, 1961, 1964, 1968, 1973, 1979). Besides the identification of the large channel bank failures, Wilderom (1979) also identified locations that are susceptible to shoal margin collapses (Figure 2a, Wilderom 1972). Over the years, especially since the completion of the Delta works in 1987, bank protection measures have been implemented to protect the outer channel banks and dikes of the Western Scheldt from new channel bank failures (Figure 2b). These measures, including periodical maintenance, appeared so effective that such large bank collapses no longer occurred. On the other hand, tidal flats and shoal margins are not essential for flood protection, so they are not protected and collapses have continued. The tidal flats in the Western Scheldt, including the shoals, have increased in height and steepness over the past decades (De Vet *et al.*, 2017), partly as a result of the protection works (Wilderom, 1972), but also as a result of more recent deepening of the main channel due to the removal of sills in the

fairway and disposal of dredged spoil in side channels and on channel margins. This results in conditions that are favorable for new collapses and stress the need for a predictor of locations, probabilities and dimensions, whereas in the Eastern Scheldt the tidal flats and shoal margins decrease in height (De Vet *et al.*, 2017) because of the reduced tidal range as a result of the installation of the Storm Surge Barrier in 1987.

## Methods

This paper evaluates the occurrence of shoal margin collapses in the Western Scheldt, particularly on characteristic geometries, spatial distribution and underlying conditions. To establish shoal margin collapse locations bathymetry data, so-called ‘Vaklodingen’, of the Western Scheldt are acquired for the period 1959–2015. After visual identification of shoal margin collapses and the spatial distribution, the displaced area and volume are calculated. The bathymetry data are then used to modify a shoal margin collapse predictor, and the accuracy of the assessment is evaluated by a receiver operating characteristic (ROC) curve.

## Identification shoal margin collapses

Shoal margin collapses were identified from existing digital elevation models (DEMs). Digital elevation models for the



Western Scheldt came from bathymetry data with a grid resolution of  $20 \times 20$  m that were measured by Rijkswaterstaat and the Flemish government for the period 1959–2015 (see example in Figure 2a). This dataset combines single beam measurements at 100/200 m transects extended with GPS real-time kinematic (RTK) measurements on top of the tidal flats (see also De Vet *et al.*, 2017). Since 2001, the dry parts of the estuaries were measured with the light detection and ranging (LiDAR) technique, the data from which was included in the bathymetry. The vertical accuracy of the bathymetry data for the  $20 \times 20$  m grid was estimated at 50 cm ( $2\sigma$ ) for the single beam and RTK data (Wiegmann *et al.*, 2005). The accuracy improved for the LiDAR data, approximately 30 cm ( $2\sigma$ ). Because of the distance between transects, which are refined on the  $20 \times 20$  m grid, some highs and lows are not detected for the single beam measurements, which means that collapses up to 200 m between consecutive transects are not visible, but otherwise collapses larger than 4000 m<sup>2</sup> could be detected. We assumed that smaller collapses did not occur as the initial scar needs a minimum size, otherwise a flow slide will not develop.

Shoal margin collapses in the Western Scheldt were identified from produced slope maps, slope difference maps and DEMs of difference (DoD) for consecutive years from 1960 to 2015. The recovery of the tidal flat of the Walsoorden collapse of 2014 was monitored in the framework of the Dutch–Flemish Western Scheldt monitoring program (Mastbergen and Schrijvershof, 2016) and data were analyzed to identify the number and frequency of thus far unnoticed shoal margin collapses in this area in the period 2000–2015 (IMDC, 2016). We used similar criteria to IMDC (2016) to identify shoal margin collapses, which were (i) focused on local erosion phenomena, and (ii) that eroded sediment should be deposited across the shoal margin, unless eroded sediment deposited in a location with a high transport capacity, e.g. main channel. The date of collapse corresponded to the bathymetry data in which the collapse was observed, i.e. the collapse occurred in the year before. IMDC (2016) determined solely the locations of shoal margin collapses for the eastern part of the Western Scheldt for the period 2000–2015, and used higher resolution and frequency multi-beam measurement near the ‘Plaat van Walsoorden’ to justify their allocated shoal margin collapses. An example of a well-studied shoal margin collapse that occurred in 2014 (Van Schaick, 2015; Mastbergen and Schrijvershof, 2016) is given in Figure 1. Despite the ability to validate the approach by well-known collapses, there remained an uncertainty in the identification of shoal margin collapses because of rapid shoal margin recovery (generally a few months) relative to the time interval between bathymetry data collection. For example, because of erosion and sedimentation at the shoal margin collapse of 2014, the original shoal margin collapse was not visible after a year (Jentink, 2015; Van den Berg *et al.*, 2017). Thus the calculated volumes from the bathymetry data are generally less than the actually displaced volume.

Shoal margin collapses were manually digitized by drawing a polygon at the boundary of the eroded part determined from the DoD. These polygons were used to determine characteristic geometric sizes and volumes of the shoal margin erosion scar. The geometry of the collapse was described by its eccentricity ( $\varepsilon$ ). The  $\varepsilon$  is a measure to determine whether the shape is circular. Specifically,  $\varepsilon = 0$  for a circle,  $0 < \varepsilon < 1$  for an ellipse,  $\varepsilon = 1$  for a parabola and  $\varepsilon > 1$  is a hyperbola. The value of  $\varepsilon$  can be calculated from the semi-major axis ( $a$ ) and semi-minor axis ( $b$ ) of the shoal margin collapse

as follows:

$$\varepsilon = \frac{\sqrt{(a^2 - b^2)}}{a} \quad (1)$$

where  $\sqrt{(a^2 - b^2)}$  is also known as the distance between the center of the polygon (circle) and each focus ( $f$ ). The volume was calculated from the difference in bed elevation between two consecutive time steps. We found that the collapsed volume of the shoal margin collapse can be approximated by a part of an ellipsoid, which has volume

$$V = \frac{4}{3}\pi abc \quad (2)$$

where  $c$  is the third semi-axis and in this study is taken to be equal to the maximum observed depth of the shoal margin collapse.

## Estuary shape and shoal margin collapses

The processes of a flow slide require sufficiently high and steep slopes. High and steep slopes are controlled by the shape of the estuary. The bending of a channel promotes a deepening of the channel, whereas bank protection works limit lateral migration of the bend. For estuaries, Leuven *et al.* (2018) showed that the summed width of shoals ( $W_b$ ), i.e. bars, approximates the excess width ( $W_e$ ) as measured in the along-channel direction for the Western Scheldt. Intuitively, this method showed and predicts shoals to fill up that part of the estuary cross-section that is not part of the minimum channel width associated with the ideal estuary. We hypothesized that shoal margin collapses occur at locations where the summed width of shoals exceeds the excess width, i.e.

$$\frac{W_b - W_e}{W_e} > 0 \quad (3)$$

Here,  $W_e$  is the excess width, defined by the active estuary width, excluding the ‘Verdrongen Land van Saeftinghe’, minus the width of the ideal exponential fit, i.e. trumpet shape of the estuary (Savenije, 2015).  $W_b$  is the summed width of shoals, defined as the sum of all shoal widths in the cross-section (Leuven *et al.*, 2018). In the case that Equation (3) is true, there are two options: (i) the channel will be pushed by the shoal to migrate laterally (Eke *et al.*, 2014; Van de Lageweg *et al.*, 2014), or (ii) alternatively, in the case of a cohesive or protected bank, the channel will deepen (Kleinhans, 2010). Where the Western Scheldt was protected by embankments the channel will deepen and shoal will accrete vertically, which would oversteepen the shoal margin, increasing the slope height and angle and making the shoal margin susceptible to collapses.

$W_e$  as well as  $W_b$  were determined by the same method as Leuven *et al.* (2018). Firstly, a centerline was defined as the mean location line between the polygon boundaries of the Western Scheldt. Secondly, the centerline was smoothed and resampled at an interval of 200 m. At all resampled points, a cross-section was constructed with a 20 m transverse grid spacing, perpendicular to the centerline and within the boundaries of the Western Scheldt. Finally, the width along the centerline of the estuary was given by the length of the successive cross-sections (Figure 3a). The  $W_b$  was calculated by extracting bathymetric profiles at the cross-sections, and the median bed elevation was determined for each cross-section (Figure 3b). Subsequently, a linear regression was fitted to the median bed elevation along the estuary channel, as the estuary depth profile often shows a linear or almost linear profile (Savenije, 2015) and the Western Scheldt is no exception (Leuven *et al.*, 2018). Elevation above the

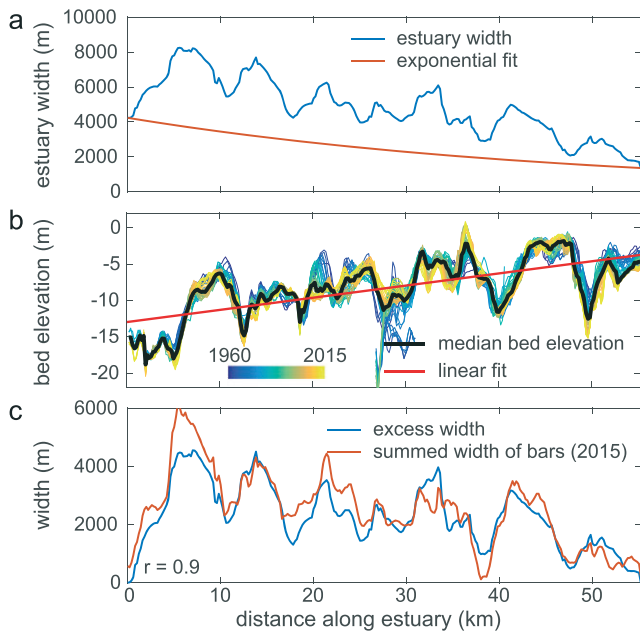


**Figure 3.** Occurrence of shoals related to estuary width. (a) Estuary width based on planform polygons for the Western Scheldt (modified from Leuven *et al.*, 2018). An exponential function is fitted on the width between the mouth and the upstream minimum river width. (b) Summed width of shoals is defined as the length over which the elevation exceeds a linear fit on the along-channel median bed elevation (Leuven *et al.*, 2018). A single fit was used for the period 1960–2015, because variations in median bed level were minor. (c) Excess width was calculated as the estuary width minus the exponential best-fit width ('trumpet shape') and compared to the measured summed width of shoals derived from bathymetries (b). The  $r$ -value indicates the correlation coefficient.

regression line was determined as shoal and  $W_b$  was determined as the total width of the bed above this regression line per cross-section (Figure 3c).

### Forecasting method to determine the probability of shoal margin collapses

Due to the limited possibilities for quantifying the influence of site characteristic geotechnical data on flow-slide probability using empirical data only, Van den Ham *et al.* (2014) pro-

posed a practical, semi-empirical method for assessing flow slide probability on a transverse profile at the channel bank, which results in a probability per kilometer per year that is representative for a (uniform) slope section with a certain length. This method is presently used to assess dike safety in the Netherlands (Deltares, 2017) and is based on statistical information about the documented historical flow slides of Wilderom (1979) per kilometer of channel banks, in which the results of complex theoretical models, describing physics of static liquefaction or breach flow slides, were incorporated. The triggering of liquefaction is strongly determined by the effective stress conditions in the saturated sand. These are determined by the steepness, height of the slope and level of the phreatic line: soil above the phreatic line has a higher weight than the submerged weight. In order to enable comparison between completely submerged slopes and slopes that are partly above the water level (phreatic line below surface level), Van den Ham *et al.* (2014) introduced a so-called fictitious slope (height in meters,  $H_f$ , and angle in degrees,  $\alpha_f$ , Figure 4a). The fictitious slope represents the actual slope, comprising an underwater part and/or an above-water part, as if it were completely submerged, in such a way that the stress conditions in the soil (sand layers) below the fictitious slope correspond to the actual stress conditions. The submerged (or buoyant) density of sand is lower than the saturated or dry density (submerged density = saturated density density of water). The lower the water level, the higher is the fictitious slope, which means that the probability of slope failure is highest at low water level (LWL). The equation for the bank safety calculation for a liquefied flow slide (Van den Ham *et al.*, 2014; Deltares, 2017) follows

$$F(\text{SC}_{\text{liquefaction}}) = \left(\frac{H_f}{24}\right)^{2.5} \cdot \left(\frac{5}{\cot \alpha_f}\right)^5 \cdot \left(\frac{1}{10}\right)^{-10(0.05+\psi)} \cdot \frac{V_{\text{local}}}{V_{\text{WS}}} \cdot \frac{\text{SC}_{\text{avg}}}{L_m} \text{ km yr}^{-1} \quad (4)$$

where  $\psi$  is the state parameter as a function of a cone penetration test according to the relation by Shuttle and Jefferies (1998), which is the average value of the state parameter in the soil layers between top and toe of the submerged slope, with a (cumulative) thickness of 5 m having the loosest packing (highest  $\psi$ ). A negative  $\psi$  indicates dense, dilative soils, whereas a positive  $\psi$  indicates loose contractive soils (see also Van Duinen *et al.*, 2014).  $\psi$  is compared to the general value of 0.05 for the Western Scheldt (Van den Ham *et al.*, 2014).  $V_{\text{local}}$  is the local bank migration rate in meters per year and

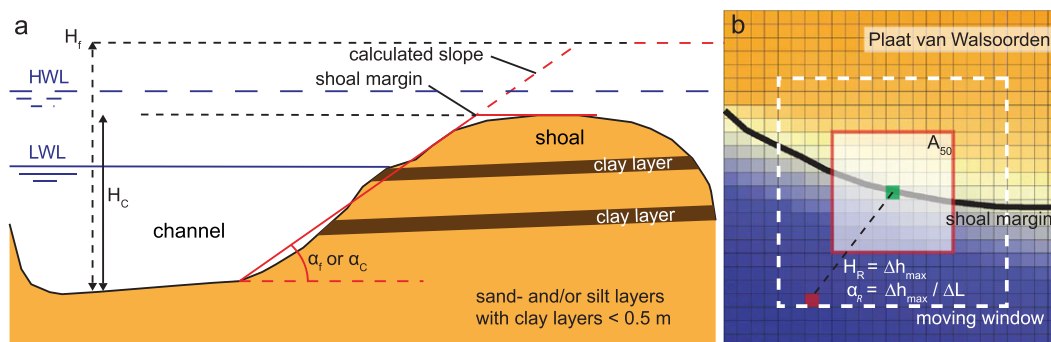


**Figure 4.** Measurements required for bank safety assessment and probability of occurrence of a shoal margin collapse. (a) Existing transect method where fictitious slope height ( $H_f$ , Equation (4)) or channel height ( $H_c$ , Equation (5)) and associated slope angle ( $\alpha_f$  or  $\alpha_c$ , Equations (4)–(5)) for the bank safety assessment are calculated across the channel (modified after Deltares, 2017). LWL stands for low water level, and HWL for high water level. (b) Our modified method to determine relative slope height and relative slope angle from the DEMs. A window is chosen that has the same size as the median shoal margin collapsed area ( $A_{50}$ ), and calculated within the window is the maximum relative slope height and the corresponding relative slope angle in an arbitrary direction.

$V_{WS}$  is the average bank migration in the Western Scheldt (1 m  $yr^{-1}$ ).  $SC_{avg}$  is the average number of collapses a year and  $L_m$  is the total length in kilometers of the margin in the Western Scheldt.  $\frac{SC_{avg}}{L_m}$  is 0.01 km  $yr^{-1}$  for the Western Scheldt (Deltares, 2017). Several of these parameters will be adapted for our shoal margin collapses assessment.

Breaching occurs when a steep scarp releases fine compacted sediment particle by particle or in thin slabs (You *et al.*, 2014; Van den Berg *et al.*, 2017). Contrary to liquefied flow slides, breaching sediment is densely packed, so that water has to infiltrate and increase pore space, i.e. dilatancy, before it can flow, which is slower for finer sand. The under-pressurized sand therefore maintains a much steeper slope than the angle of repose, which slowly retrogresses, defined by permeability. The equation for the bank safety calculation for breaching (Van den Ham *et al.*, 2014; Deltares, 2017) follows

$$F(SC_{breach}) = \left(\frac{H_C}{24}\right)^5 \cdot \left(\frac{5}{\cot \alpha_C}\right)^5 \cdot \left(\frac{2 \cdot 10^{-4}}{D_{50}}\right)^5 \cdot Fr_{clay} \cdot \frac{V_{local}}{V_{WS}} \cdot \frac{SC_{avg}}{L_m} \text{ km yr}^{-1} \quad (5)$$

where  $H_C$  is the channel depth in meters,  $\alpha_C$  is the associated slope angle,  $D_{50}$  is the averaged grain size in meters over all sand layers between top and toe of the submerged slope, and is divided by the median grain size, which is considered critical for breach flow slide ( $2 \times 10^{-4}$  m).  $Fr_{clay}$  is a factor for the thin clay layers, where  $Fr_{clay}$  is 1/3 for absence of thin clay layers and  $Fr_{clay}$  is 3 for many thin clay layers. The database of Wilderom (1979) mainly included flow slides at channel banks, for obvious reasons of dike safety. We assumed that the conditions for flow slides on the shoals should be the same and that this bank safety assessment of Deltares (2017) could be applicable as a forecasting method for the less steep shoal margins as well, with some adjustment from our analysis of the collapse conditions.

For this study we used the same height for breaching and liquefaction (thus  $H_f = H_C$ ), because the majority of slopes of the shoals are completely submerged compared to outer bank slopes for the original prediction (Figure 4a). We modified the calculation of the slope  $H$  to make it applicable to spatial bathymetry data. A relative slope height,  $H_R$ , was determined for each grid cell by determining the maximum height difference ( $\Delta h_{max}$ ) from the center to the deeper deepest bottom level within a window. Here,  $H_R$  was in the range of  $H_C$  as this only takes account of the height difference between two points instead of adding a fictitious slope geometry that contributes to the stress. A relative slope angle,  $\alpha_R$ , was then calculated as the angle between the cells with  $\Delta h_{max}$  and their distance ( $\Delta L$ ; Figure 4b). For the window size we used the median size of the shoal margin collapses ( $A_{50}$ ), but we also tested the sensitivity of the window size on the probability values.

The bathymetry data enable quantification of the spatial variation in the slope height ( $H$ ) and angle ( $\alpha$ ) for Equations (4) and (5). Because of the lack in spatial information and the distribution for the variables  $D_{50}$ ,  $\psi$  and  $Fr_{clay}$ , fixed values were considered corresponding to the average values for the Western Scheldt of  $2 \times 10^{-4}$  m,  $-0.05$  and  $1$ , respectively (Van den Ham *et al.*, 2014). Although Van den Berg *et al.* (2017) argued that collapse of the slopes was dominated by breaching, there is no information on the actual process. Therefore, we considered that half of all flow slides were pure liquefaction flow slides, while the other half concerned pure breach flow slides (Van den Ham *et al.*, 2014; Van Duinen *et al.*, 2014; Deltares, 2017). Eventually, the bank safety assessment could be written

as follows:

$$F_{SC} = \left[ 0.5 \left(\frac{H_R}{24}\right)^{2.5} \left(\frac{5}{\cot \alpha_R}\right)^5 + 0.5 \left(\frac{H_R}{24}\right)^5 \left(\frac{5}{\cot \alpha_R}\right)^5 \right] \cdot \frac{V_{local}}{V_{WS}} \text{ km yr}^{-1} \quad (6)$$

where the other variables are excluded, as these are considered to be constant within the Western Scheldt. The form of Equation (6) allows frequency to be higher than 1, which was prevented by a transformation, namely a Poisson process, of the frequency into a probability ( $P(FS)$ ):

$$P_{SC} = 1 - e^{-F_{SC}} \quad (7)$$

Initially we excluded the spatial variation in  $Fr_{clay}$  and  $\psi$  and applied a constant value because of the lack of spatial information. Later, we extended the shoal margin collapse predictor to include a spatial variable  $Fr_{clay}$  (Equation (5)) and  $\psi$  (Equation (4)) because these variables might improve the predicted shoal margin collapse locations. However, as spatial data for these variables were unavailable, some assumptions had to be made for a tentative test. The first assumption was that information about the spatial distribution of clay probability could give an indication for spatial variation in clay layers. We assumed that the distribution of clay has not changed significantly over the past within the shoals and that the clay fraction measured at the surface is a first-order estimate for the amount of thin clay layers within the submerged slope, for lack of more information. The surface samples might be unrealistic as the clay fraction settles at high water slack, while the deeper shoal had a more energetic environment that prevented settling of clay during deposition. We used the dataset from the GeoTOP model of TNO (2016), which provided information about the probability that the lithological unit clay was found within a grid cell of  $100 \times 100$  m for the top 50 cm (see also Braat *et al.*, 2017). A value for  $Fr_{clay}$  was assigned based on the probability of clay for TNO (2016) data, where  $Fr_{clay} = 1/3$  for less than the median,  $Fr_{clay} = 1$  for locations equal to the median, and  $Fr_{clay} = 3$  for locations with more than the median.

The second assumption was that the age of the deposits determines the state parameter,  $\psi$ . We assumed that aged sands became more resistant with time because of consolidation (Biot, 1941) due to cementation and compressibility, and that  $\psi$  increased lognormally for the saturated sediments with the age of the deposit (Hayati and Andrus, 2009).  $\psi$  was determined by the subsurface of the submerged slopes. In earlier work, the subsurface was described by three stratigraphic units (Wilderom, 1979): (i) 'Jong Zeezand', i.e. Subatlantic fine sand deposits (after 2500 yr BP), (ii) 'Oud Zeezand', i.e. Atlantic fine sand deposits (before 2500 yr BP): and (iii) Pleistocene sand deposits (before 11 700 yr BP). Both Subatlantic sands and Atlantic sands concern tidal deposits, although from different age, and were deposited very quickly, resulting in very low densities during deposition. The estimated average  $\psi$  varies for these various stratigraphic units between 0,  $-0.05$  and  $-0.1$  for Subatlantic sand, Atlantic sand and Pleistocene sand, respectively. In this study, a  $\psi$  was assumed based on the age of the deposits for the top 5 m, where the oldest deposits (deposited in 1959) had a  $\psi$  value of  $-0.05$  and the youngest deposits (deposited in 2015) had a  $\psi$  value of 0. A lognormal function, i.e.  $\psi_T = -0.0125 \log(2015 - T)$  with  $T$  the year of deposit, was applied between the youngest and oldest sediments to determine a state parameter for sediment ages ( $\psi_T$ ), which was then multiplied by its fraction ( $f_T$ ) within the top

5 m of the deposits. The spatial variable state parameter ( $\Psi_{T5}$ ) follows as

$$\Psi_{T5} = \sum_{T=1}^{55} f_T \psi_T \quad (8)$$

where  $T$  is year of the sediment deposition, with  $T = 0$  for 1959.  $f_T$  is the fraction of deposited sediment for year  $T$  in the top 5 m.

Finally in the discussion, we performed a multi-regression analysis on the various variables and test whether the forecasting method for shoal margin collapses can be improved. Additionally, a multi-regression analysis is performed on the variables to determine the shoal margin collapse size and volumes. In the discussion, we also provided several equations for determining the geometric dimension, i.e. the axis  $abc$ , of the shoal margin collapses, which can be included in a numerical morphodynamic model.

### Validation of the forecasting method by receiver operating characteristics

The forecasting method returned a probability map of shoal margin collapses for the Western Scheldt. To quantitatively compare these probability maps with binary values of [0, 1] for locations without or with shoal margin collapse, we calculated an ROC curve. This curve indicates the performance of a binary classifier system (in this case, shoal margin collapses) as the threshold for the probability of a collapse ( $P_{SC}$ ) is varied (see also explanation in Van Dijk *et al.*, 2016). The curve was constructed by plotting the true positive rate (TPR), defined as the number of cells that had shoal margin collapses in both the predictive probability and observed collapses divided by the number of observed locations of collapses, against the false positive rate (FPR), defined as the number of cells that had shoal margin collapses in the predictive probability but no observations of collapses divided by the number of cells with no shoal margin collapse observations. The TPR and FPR were calculated for various threshold values of the probability ( $P_{SC}$ ). Increasing the threshold for the probability led to fewer cells being classified as locations of shoal margin collapses, and should lead to a decrease in both TPR and FPR. ROC curves were constructed for various window sizes, and for the shoal margin collapses prediction, which includes the spatial variation of clay or relative density. An effective model should show a higher TPR at a given FPR than random prediction, which was summarized by the area under the ROC curve (AUC):

$$AUC = \int_{-\infty}^{\infty} TPR(D)FPR'(D)dD \quad (9)$$

where  $D$  is the given threshold parameter, and it is assumed that 'positive' ranks higher than 'negative'. The AUC measures discrimination, i.e. the ability of the test to correctly classify location with and without shoal margin collapses. The AUC is the percentage of randomly drawn pairs for which the test correctly predicts the shoal margin locations. A random predictor will give an AUC of 0.5, whereas an excellent predictor will give an AUC of 0.9–1.0.

## Results

### Shoal margin collapses

Analysis of consecutive bathymetry data enables us to distinguish a total of 299 shoal margin collapses in the period 1959–2015 (Figures 2a and 5a). This means that on average 5.3 collapses ( $SC_{avg}$ ) occur per year in the Western Scheldt. The 299 shoal margin collapses that are identified included mainly collapses at the shoal margins and only a few at the

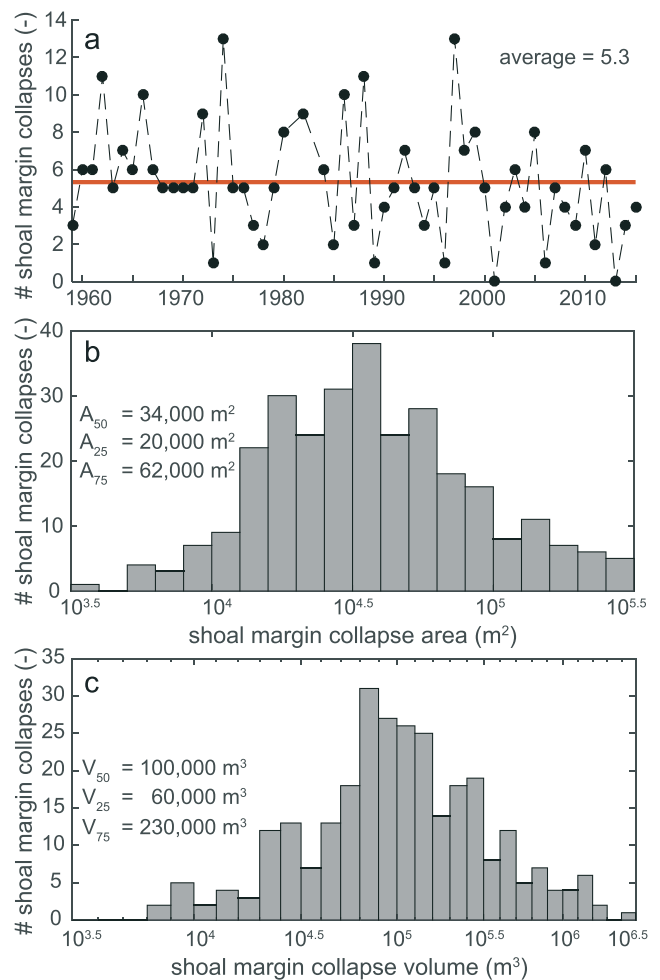


**Figure 5.** Number, size and volume of shoal margin collapses for the period 1960–2015. (a) The yearly average number of shoal margin collapses is 5.3 and decays over the years according to a linear regression of  $-0.057 \text{ years} + 7.096$ . (b) The size of the shoal margin collapses varies from the smallest of  $4000 \text{ m}^2$  up to  $300\,000 \text{ m}^2$ , but half of the collapses cover an area between  $20\,000$  and  $62\,000 \text{ m}^2$ . (c) The volume of the shoal margin collapses varies from  $6000 \text{ m}^3$  up to  $3 \times 10^6 \text{ m}^3$ , whereas the median is about  $100\,000 \text{ m}^3$ .

channel banks. From the fitted regression line for the median depth along the estuary, shoal margins were distinguished and the migration of the shoals were tracked in the Western Scheldt (Figure 2b). The total measured shoal margin length ( $L_m$ ), excluding the channel banks, is  $300 \text{ km}$  for the Western Scheldt. The size of the collapses varies from about  $4000$  to  $300\,000 \text{ m}^2$ , with a median size of  $34\,000 \text{ m}^2$  (Figure 5b). The shoal margin collapse sizes are lognormally distributed, with a mean  $\mu$  of  $10.38$  and a standard deviation  $\sigma$  of  $0.88$  with a skewness of  $2.26$ . The volume of the collapses varies from  $6000 \text{ m}^3$  to  $3 \times 10^6 \text{ m}^3$ , with a median volume of  $100\,000 \text{ m}^3$ . The shoal margin collapse volume is also lognormally distributed, with a mean  $\mu$  of  $11.59$  and a standard deviation  $\sigma$  of  $1.21$ , with a skewness of  $3.56$ . These values are minimum values, because collapsed gaps likely silted up partly before the sounding date of detection.

The shape of the shoal margin collapses is described by the three semi-axes  $abc$ . In general, the semi-axes  $a$  and  $b$  are not equal (Figure 6a). Analysis of both lengths show that even for the longest and widest collapses axis  $c$ , i.e. the thickness, does not scale with the size of the collapse. The eccentricity ( $\varepsilon$ ) indicates that the planform shape of collapses is not circular ( $\varepsilon = 0$ ) but more likely to have an elliptical shape,



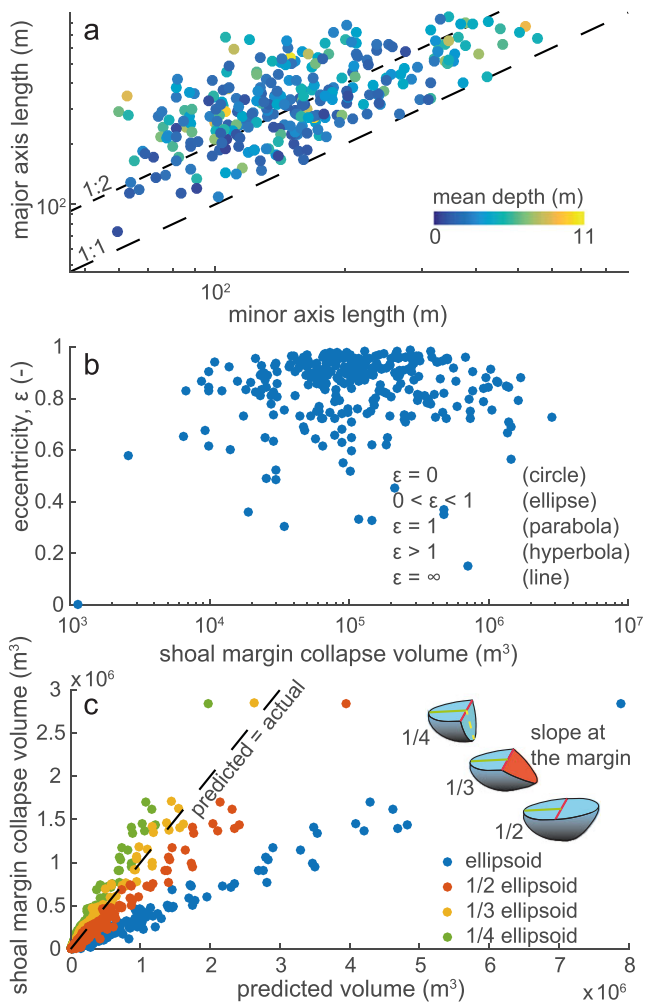


**Figure 6.** Geometry of all shoal margin collapses. (a) The collapses are not rounded in shape, but the major axis is generally twice the length of the minor axis (equality line indicated). Colors indicate the measured depth of the eroded scar, which is uncorrelated with surface minor and major axis. (b) Eccentricity of the collapses indicates that the shoal margin collapses have an ellipse planform shape that is closer to a parabola than to a perfect circle. There is no relation between the shape of the collapse and the volume. (c) The 3D geometrical shape is best predicted by 1/3 of the volume of a perfect ellipsoid, probably because of the slope at the shoal margin.

with  $\varepsilon$  mostly between 0.8 and 1 (Figure 6b), where an  $\varepsilon$  of 1 indicates a parabolic shape. The volume of the shoal margin collapses are best predicted by 1/3 of an ellipsoid, probably because of the slope at the shoal margin (see Figure 6c).

Sediment deposition volume mirrors the sediment erosion volume over time and both vary along the Western Scheldt. The total eroded sediment volume, which is a summation of the yearly eroded sediment volume calculated from the DoD, is more or less the same as the total accreted sediment volume (Figure 7a). A high volume of sediment erosion is visible around the tidal flat 'Hooge Platen' (G in Figure 2a) near the estuary mouth, and between Terneuzen and the 'Platen van Ossenisse' (D in Figure 2a). Shoal margin collapses occur along the full length of the Western Scheldt (Figure 7a), but several peaks in the eroded volume correspond to locations with multiple shoal margin collapses, indicating a local disturbance of sediment input. However, the volume of the shoal margin collapses are relatively small compared to the total eroded sediment volume for the period 1959–2015. Furthermore, the peak of eroded sediment volume between 21 and 26 km (Terneuzen and the 'Platen van Ossenisse') does not

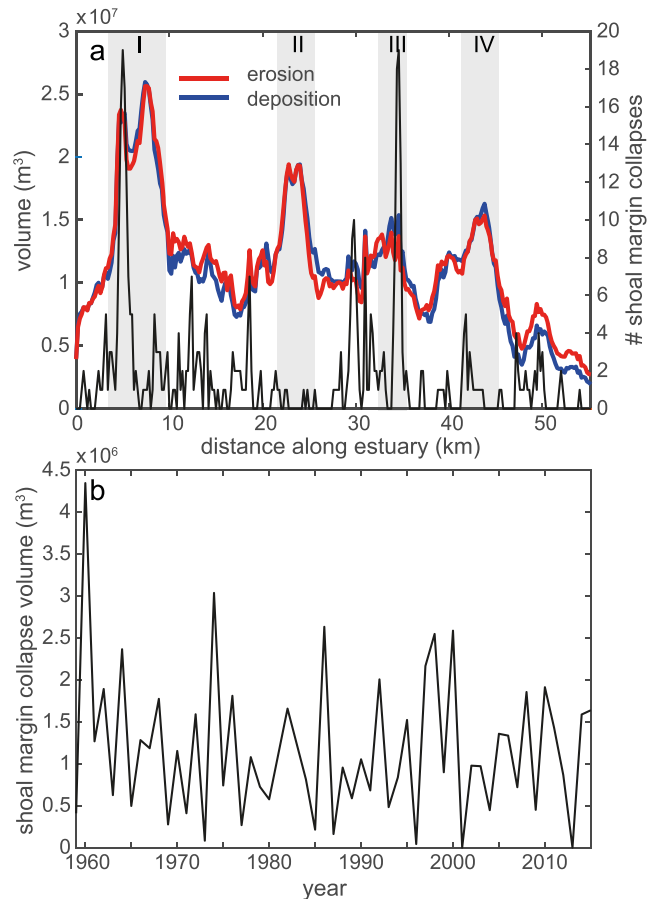


**Figure 7.** (a) Summed erosion and deposition from the yearly DoD plotted against the summed shoal margin collapse occurrence along the Western Scheldt show that deposition equals erosion, and several regions (I and III) correspond to high erosion and deposition volumes and shoal margin collapse occurrence, whereas others did not (II and IV). Furthermore, several local peaks within regions with relatively less erosion and deposition correspond to the locations of shoal margin collapses, e.g. 14, 19, 30, 31 and 50 km. (b) Summed sediment volume moved by shoal margin collapses is only a small percentage (2%) of the total eroded sediment volume in part (a).

correspond to a peak in the number of shoal margin collapses. In conclusion, over the period 1959–2015 only 2% of the total eroded sediment volume is made up by the volume of the shoal margin collapses (Figure 7b).

We hypothesized that the location of the shoal margin collapses could relate to a normalized summed width of shoals,  $W_b$ . Analysis of the shoal margin collapses along the Western Scheldt against the summed width of shoals suggests that generally collapses occur when  $(W_b - W_e)/W_e > 0$  (Figure 8a). However, there is no direct relation between the number of collapses at a cross-section and the value for  $(W_b - W_e)/W_e$  along the Western Scheldt (Figure 8b). Also, when  $(W_b - W_e)/W_e$  is larger than 0 in some cross-sections, no shoal margin collapses occurred. In other words, shoal margin failures are not linked with locations that consist of more shoals than expected. Particularly, between Terneuzen and the 'Platen van Ossenisse' around 25 km from the mouth no shoal margin collapses occurred, even with a  $(W_b - W_e)/W_e$  of 0.5. This corresponds to the same location where the volume of sediment erosion and deposition is relatively high (Figure 7a). Analysis of the variation in the summed width of shoals, as indicator for the migration rate, shows that the variation is not significantly higher for locations with shoal margin collapses (Figure 8c). There-



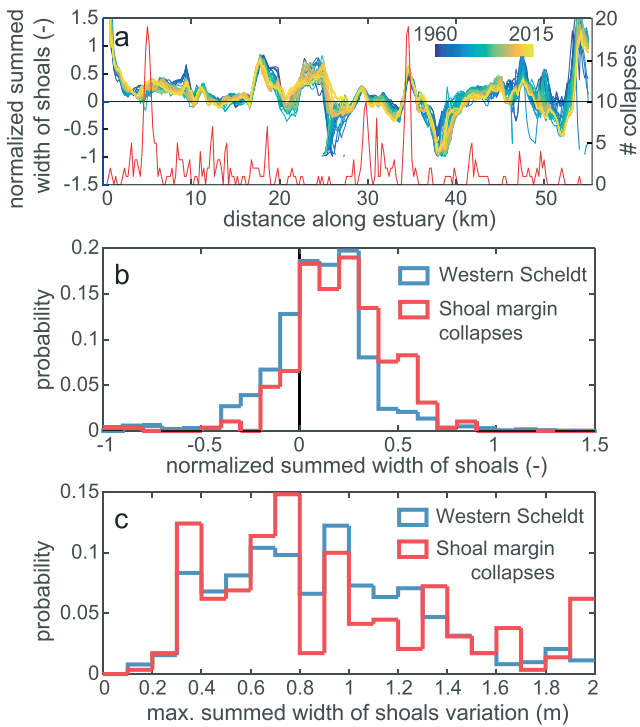


**Figure 8.** Correlation between variation in summed width of shoals relative to excess estuary width and occurrence of shoal margin collapses. (a) Normalized summed width of shoals plotted against the shoal margin collapse locations along the Western Scheldt. Note that the highest peaks in the number of shoal margin collapses correspond to locations with normalized summed width of shoals greater than 0, but not all locations where normalized summed width of shoals is larger than 0 have excessive shoal margin collapses. (b) Distribution of the probability of the normalized summed width of shoals shows that for shoal margin collapses the value is mostly above 0 and higher than for the value of the entire Western Scheldt. Note that most collapses occur at locations with a value larger than 0, but shoal margin collapses also occur for locations with values less than 0. (c) Distribution of the variation in summed width of shoals, i.e. migration rate, shows no significant difference between locations with and without shoal margin collapses in the Western Scheldt.

fore, for the forecasting method of the shoal margin collapses we excluded the factor  $V_{\text{local}}/V_{\text{WVS}}$  in Equations (4)–(6) and suggest that lateral migration rate is instead relative low for locations with shoal margin collapses as collapses recur at the same location probably because of fixation of the estuary margin by embankments.

### Shoal margin collapse assessment

The probability of shoal margin collapses From the bathymetry data the relative slope height and angle are calculated, which are applied in the forecasting method to determine the probability of shoal margin collapses. In the initial calculations a constant value was taken for  $\psi$  and  $Fr_{\text{clay}}$  of  $-0.05$  and  $1$ , respectively, that represents the mean in the Western Scheldt.  $SC_{\text{avg}}$  and  $L_m$  of  $5.3$  and  $300$  km, respectively, are calculated for the Western Scheldt, whereas the variables  $V_{\text{local}}$  and  $V_{\text{WVS}}$  are excluded from the forecasting method (see previous section). Because of the spatial information of the bathymetry, a spatial probability map is generated that predicts the probability of a shoal margin collapse in the Western Scheldt.

Figure 9(a) shows the variation in the relative slope height for the Western Scheldt in 2015. The shoal margins and channel banks have a typical value of  $H_R > 1$ , while the channels

and shoals itself have a value of less than  $1$  m. The histogram of the probability illustrates that most values are less than  $5$  m for the Western Scheldt and the shoal margins, but that for the locations with shoal margin collapses it is more likely to have an  $H_R$  of more than  $5$  m (Figure 9b). The median height ( $H_{R,50}$ ) for the shoal margin collapses is  $11$  m. The spatial map of  $\alpha_R$  (Figure 9c) shows that a major part of the Western Scheldt has an  $\alpha_R < 1^\circ$ , i.e.  $\cot(\alpha_R) = 45$  (Figure 9d), and a steeper  $\alpha_R$  corresponds to higher  $H_R$  values. The histogram of the probability illustrates that most slopes are steeper than  $3^\circ$ , i.e.  $\cot(\alpha_R) = 19$ , for the shoal margin collapses, whereas the general slope of the shoal margins is less than  $3^\circ$ .

$H_R$  and  $\alpha_R$  combined in the shoal margin collapse predictor shows spatial variation in the probability along the shoal margins (Figure 9e). Bank protection measures on the northern but mainly southern banks of the Western Scheldt correspond to locations with high probabilities, and therefore the analysis focuses mainly on the shoal margins. Also high probabilities are found at the edge of the shallower part between Vlissingen and Borsello (so-called ‘Honte’). Migration of the deeper part (below  $-24$  m NAP = Amsterdam Ordnance Datum) in the ‘Honte’ of the Western Scheldt was slower than the shallower part (above  $-24$  m NAP), which led to the development of a plateau at a depth of  $-24$  m NAP. This plateau is insusceptible to shoal margin collapses, because of the resistant layer formed by shell deposits (so-called ‘crags’; Cleveringa, 2013). Calculation of the probability shows different outcomes for shoal margin collapses by breaching and liquefaction (Figure 9f). In general, the probabilities for breaching are lower compared to liquefaction. A combined probability (Equation (6)) gives probability values (almost) comparable to probabilities for liquefaction. Variation in the window sizes shows that with a larger window size ( $300 \times 300$  m) than the average collapse size ( $A_{50}$ ) the probabilities hardly increased, mainly because the increase in  $H_R$  was counteracted by a decrease in  $\alpha_R$  (Figure 9f).

### Role of spatial variation of clay layers and state parameter on the assessment

In the initial calculation for the probability we assumed a constant value for  $Fr_{\text{clay}}$  and  $\psi$ , whereas it is more likely that these vary spatially as well. The GeoTOP model of clay probability is used to assess whether the spatial variation of clay associated with thin clay layers improves the prediction of the shoal margin collapse locations. The spatial distribution of clay probability from the GeoTOP model (Figure 10a) shows that for most locations with shoal margin collapses the clay probability is higher than the average probability (Figure 10b).

The bathymetry data are used to estimate a spatial distribution of state parameter ( $\Psi_{T5}$ ) based on the relative age. From consecutive bathymetry data it is noticed that the relative age of the surface is actually young for most tidal flats/shoals (Figure 10c). This is also true for the ages of the collapsed shoal margin sediments. Most eroded sediment has been reworked within  $10$  years (Figure 10d), which is determined by the age difference between two consecutive years of the surface maps. The  $\Psi_{T5}$  value is determined by the age of the top  $5$  m of the deposits, and shows relatively high values at the shoal margin and in the secondary channels that are slowly filling up for 2015 (Figure 10e). The proposed  $\Psi_{T5}$  identifies large areas with a  $\Psi_{T5}$  closer to  $-0.05$ , i.e. deposited in 1959, whereas the locations with shoal margin collapses have generally a  $\Psi_{T5}$  value higher than  $-0.05$ , i.e. closer to deposits from 2015 (Figure 10f). In general, this indicates that shoal margin collapses mainly occur at locations with young ‘loosely packed’ deposits. Because the age of the deposits that were eroded is younger than  $10$  years, we argue that the generated  $\Psi_{T5}$  map

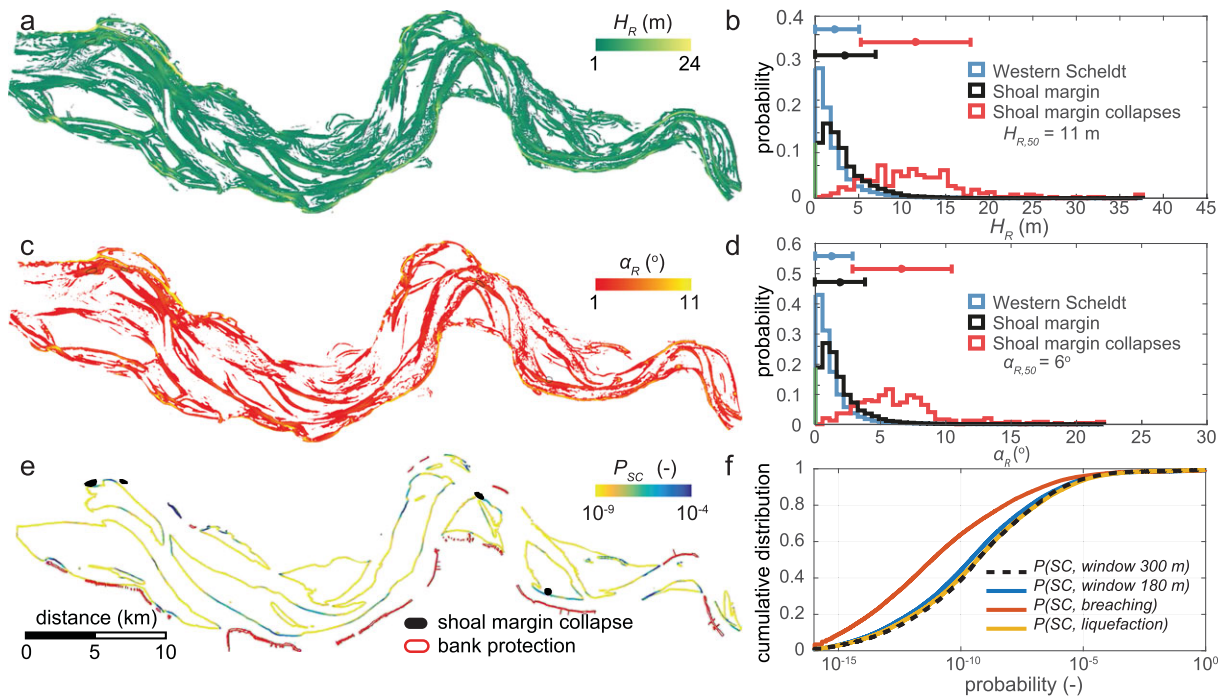


**Figure 9.** Example of predicted probability of shoal margin collapses. (a)  $H_R$  map shows the highest slopes at the outer banks of the estuary for the Western Scheldt in 2015. (b) Distribution of  $H_R$  for the shoal margin collapse locations shows that the median slope height before the collapse was 11 m, which is about the median water depth of 15 m. (c) The  $\alpha_R$  map shows that the steepest slopes are located at the same locations as the highest slopes in part (a) for the Western Scheldt in 2015. (d) Distribution of  $\alpha_R$  for the shoal margin collapse locations illustrates that the angle was  $6^\circ$ , i.e.  $\tan(\alpha_r) = 1:10$  or  $\cot(\alpha_r) = 9.5$ . (e) Probability map for the shoal margin collapses shows variation in the likelihood of a collapse along the shoal margin. (f) Cumulative distribution of the probability maps when assumed formed by breaching or by liquefaction for various failure mechanisms illustrates that flow slides according to Equation (4) for liquefaction have a considerably higher probability than flow slides formed by breaching according to Equation (5). The combined probability of Equation (6) shows that an increasing window size does not increase the probabilities significantly, because of the inverse response of the relative slope angle by an increase in the relative slope height.

of 2015 could be used to determine a  $\psi$  value for the forecasting method. Generated  $\Psi_{T5}$  maps for each single time step shows that about 30% of the collapses occurred on the initial bathymetry of 1959. However, as there is no actual age of deposition for sediments deposited before 1959, we decided to exclude these locations from the probability distribution of  $\Psi_{T5}$ . Without these locations the distribution is more comparable to the distribution for collapses based on the 2015  $\Psi_{T5}$  map than the overall distribution of  $\Psi_{T5}$  for the Western Scheldt (Figure 10f).

Accuracy of the probability of shoal margin collapses  
Receiver Operator Characteristic (ROC) curves allow us to examine the probability of shoal margin collapses and the effect of a threshold on the accuracy between the predicted locations and the actual shoal margin collapse locations. The ROC curve probabilities are calculated only for the shoal margins, because the forecasting method showed that there is a high chance for collapses to occur also for the channel banks, but these parts are protected from collapses and thus would result in a higher false positive rate (FPR). In the case of random prediction, increasing the threshold (i.e. increasing the probability value needed to assign shoal margin collapses in the final map) causes a proportionate decrease in both true positive rate (TPR) and FPR. This is represented by the straight line in Figure 11. Overall, the shoal margin forecasting method performs better for increasing threshold values, as shown by the increasing ratio of TPR to FPR (Figure 11a). The range in Figure 11(a) represents the outcomes from using bathymetry data of different years with a map of shoal margin collapse occurrences. The ratio of TPR to FPR is higher for the window size of 300 m, meaning that a large window is better in

predicting a spatial variation that translates into more accurate prediction of the shoal margin collapse locations. The area under the ROC curve (AUC) varies from around 0.7 for the older bathymetry data to 0.8 for the bathymetry data of the last decade, meaning that the increased precision of the bathymetry data predictions become more accurate. A probability threshold of about  $10^{-7}$  is sufficient to predict at least half of the shoal margin collapse locations, while FPR remains low. Keep in mind that because only 7% of the shoal margin collapsed and not 50% of the shoal margin, at the threshold of  $10^{-7}$  the FPR might be lower than the TPR, but in absolute numbers more locations are falsely identified than correctly as a location that had a shoal margin collapse.

Including spatial variation of clay or the relative age did not increase the quality of the prediction. We suspect that the inclusion of  $Fr_{clay}$  based on the GeoTOP model would not affect the prediction of the shoal margin collapse locations as there is no significant change between the distribution of the shoal margin collapses and other locations of the Western Scheldt (Figure 10b). The GeoTOP data, with an equal distribution (Figure 10b), shows no change in the prediction according to the ROC curve (Figure 11b). This implies that the current clay probability maps are not sufficient in predicting the spatial variation in clay layers or that the role of clay layers in the occurrence of shoal margin collapses could be neglected. Including a spatial state parameter ( $\Psi_{T5}$ ), whose distribution differs between the shoal margin collapse location and the Western Scheldt (Figure 10e), does not show a significant change in the improvement of the prediction in the ROC curve (Figure 11b). This suggests that although a spatial variable  $\Psi_{T5}$ , its role on predicting shoal margin collapses is insignificant in the current Equation (4), and that the

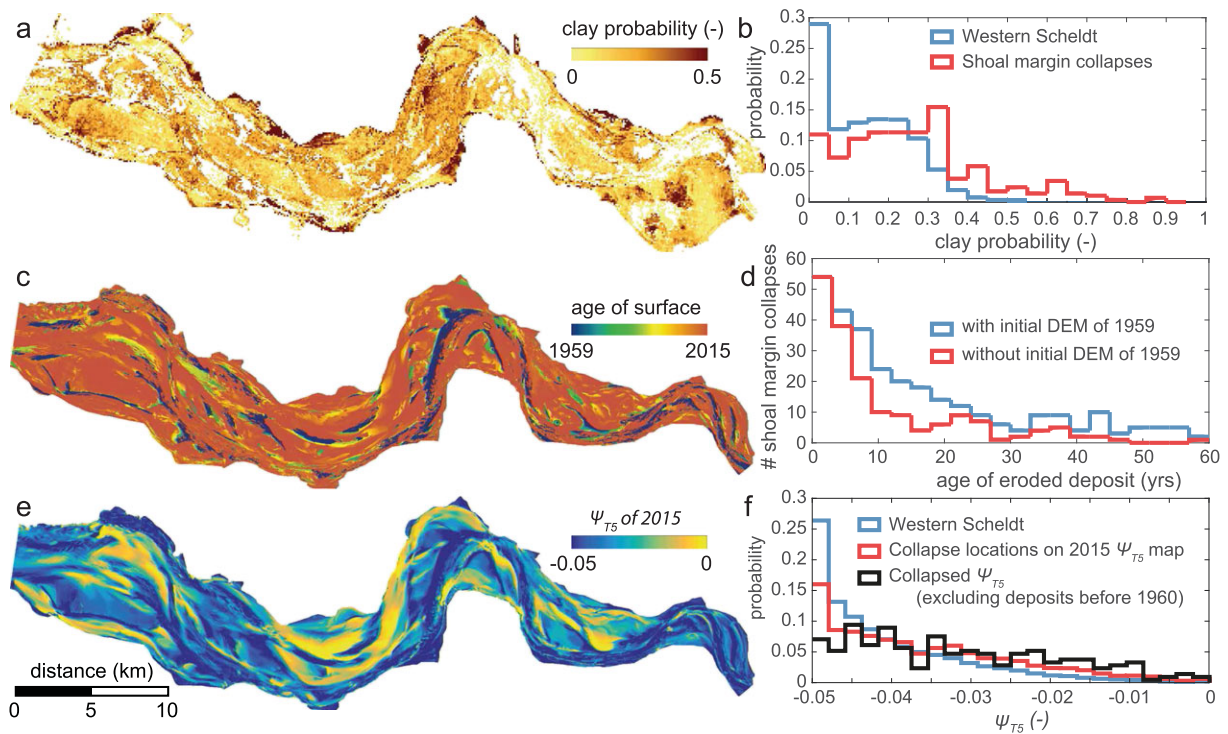


**Figure 10.** Test of dependence of collapse locations with maps of clay layer ( $F_{r_{clay}}$ ) and state parameter ( $\Psi_{TS}$ ). (a) Clay probability distribution in the Western Scheldt according to the GeoTOP model (TNO, 2016). (b) Distribution of the clay probability of the Western Scheldt and shoal margin collapse locations illustrates a minor shift of the probability distribution for locations with collapses, which indicates a minor influence of clay content. (c) Age of the surface deposit calculated from consecutive bathymetry data shows that sediment on the shoals is relative young. (d) Age distribution for the shoal margin collapse locations illustrates that the age of the eroded deposit for 50% of the collapses was younger than 10 years. (e) Assumed state parameter ( $\psi$ ) map based on a linear regression of the age for the top 5 m deposit. (f) Distribution of the state parameter shows that for the shoal margin collapse locations the probability is different than the overall Western Scheldt distribution of the state parameter. Note that we excluded shoal margin collapse locations that eroded sediments deposited before 1959.

probability is mainly determined by the variation in relative slope height and angle.

## Discussion

This study characterized the spatial distribution and geometries of shoal margin collapses in the Western Scheldt for 1959–2015 and tested a spatial forecasting method on the basis of bathymetric data. Below, we discuss our observations in comparison to an earlier study of Wilderom (1979). We also propose modification of the forecasting method based on our observations and compare the accuracy with the tested forecasting method. Finally, we consider the implication of the forecasting method for numerical modeling.

### Comparison with Wilderom (1972)

The present study of shoal margin collapses in the Western Scheldt, based on digitized bathymetry data from 1959 to 2015, actually provides an update of the database of Wilderom (1979), enabling us to update statistical data on location, geometry and occurrence intervals of this type of collapse (flow slides). It is surprising that such a large number of shoal margin collapses could be detected from the data, since it was hardly publicly known or observed. In general, the process remains completely under water. Also, large collapses were detected in the Eastern Scheldt bathymetry data but remained unnoticed for years (De Groot and Mastbergen, 2006). The large shoal margin collapse at the tidal flat of Walsoorden in 2014, however, created a large erosion scar above

the low water level of the shoal and thereby generated much public attention.

Our analysis of shoal margin collapses overlaps with the observations of Wilderom (1972) for the period 1959–1972. Wilderom (1972) describes shoal margin collapses at several tidal flats in the Western Scheldt (see Figure 2a); the ‘Spijkerplaat’ west (A) and east (B), ‘Plaat van Walsoorden’ (C), ‘Platen van Ossensisse’ (D), ‘Middelplaat’ (E) and ‘Brouwersplaat’ (F). Our study indicates that besides these tidal flats also shoal margin failure occurs at the shoals of ‘Hooge Platen’ (G) and at the shoals north of the ‘Verdronken Land van Saeftinghe’ (H). We were not able to identify all shoal margin collapses of Wilderom (1972) that were specifically mentioned. For example, the collapse in 1964 of  $3.5 \times 10^6 \text{ m}^3$  at the eastern part of the ‘Spijkerplaat’ was not detected as we missed bathymetry for this part of the Western Scheldt for 1965. We also argue that the volumes that we observed are conservative and likely underestimated, because the yearly intervals between subsequent bathymetries can cause reworking and infilling of the collapse.

Our interpretation of the bathymetry indicates changes in shoal margin collapses for the several tidal flats compared to the observations of Wilderom (1972). At the ‘Spijkerplaat’ no major collapses occur at the east side after 1970, while the west side of the ‘Spijkerplaat’ remains very active, with collapses in the three years. The western part of ‘Plaat van Walsoorden’ that was subjugated to erosion according to Wilderom (1972) became less active after shortening of the groyne near the town of Walsoorden, but the southern part of the tidal flat became susceptible to shoal margins in the last decade, showing several large shoal margin collapses (Van Schaick, 2015; Van den Berg, *et al.*, 2017). The ‘Platen van



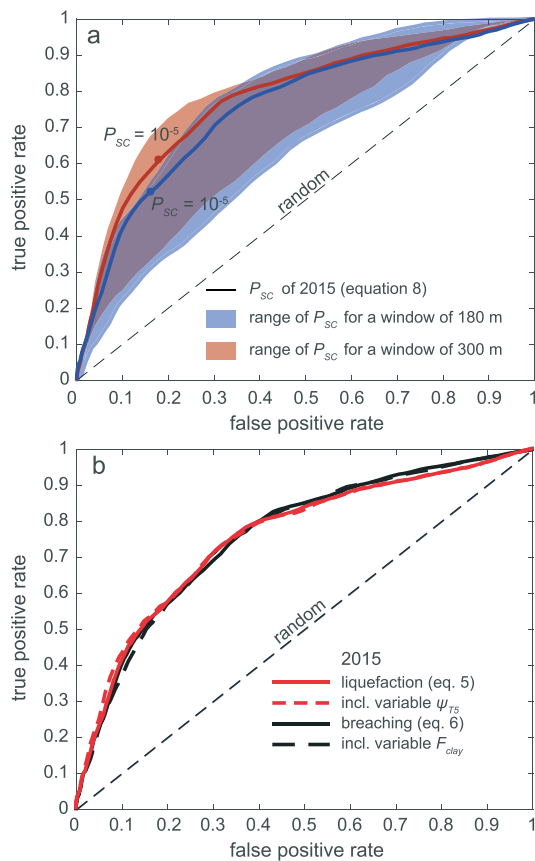


**Figure 11.** ROC curve, i.e. the FPR versus the TPR, shows that the predicted probabilities by Equation (7) are better than simply randomly selecting shoal margin locations. (a) Lower probabilities by a large window size (Figure 9f) lead to an improved prediction indicated by the ROC curve. At a probability value of  $10^{-7}$  the TPR is twice as large as the FPR, and at least 50% of the shoal margin collapse locations are predicted. (b) ROC curve for the 2015 situation shows that including a spatial  $\Psi_{T5}$  or  $Fr_{clay}$  does not improve the prediction for liquefaction or breaching, respectively.

Ossensisse' have the most shoal margin collapses over time, in agreement with Wilderom (1972). The shoal margin collapses at the 'Middelplaat', however, are less clearly defined from the bathymetry and the specific collapses of Wilderom (1972), are not detected; probably, because of general deepening of the channel, the conditions do not follow our criteria (see Methods section). Also the specific collapse at the 'Brouwersplaat' is not detected, although we do observe several shoal margin collapses after 1970. In general, the locations for shoal margin collapses reported by Wilderom (1972) and this study coincide with the higher probabilities from the forecasting method.

### Forecasting method to determine the probability of shoal margin collapses

The current forecasting method provides a tool to estimate the probability of expected collapses at banks and shoals. The current analysis indicates that the variables relative height ( $H_R$ ) and angle ( $\alpha_R$ ) are the major contributors to the frequency as well as the probability value. The current predicted frequency for shoal margin collapses is low, because  $H_R$  is divided by 24, which is based on the average height for channel bank collapses in the Western Scheldt. But also the variable  $\alpha_R$  is based on an average value of  $\cot \alpha_R$  of 5 for channel bank collapses. However, our analysis for the shoal margin collapses shows an

average height of 11 m ( $H_R$ ) and an average slope of  $6^\circ$  ( $\alpha_R$ , i.e.  $\cot \alpha_R$  of 9.5). Changing the values 24 and 5 into 11 and 9.5 in Equation (6), respectively, will increase the predicted frequency but not the accuracy of the predicted locations. Our findings suggest that the proposed  $\Psi_{T5}$ , based on age of deposition, for the shoal margin collapse locations is different from the constant  $\psi$  used for the Western Scheldt, and could improve the prediction. A multiple regression analysis, however, shows that there is not much correlation between the slope height, angle and state parameter towards the frequency of collapses, as also suggested by Van den Ham *et al.* (2014) for the historical data of Wilderom (1979).

In general, shoal margin failures mainly occur at locations with young 'loosely packed' deposits, preferable at locations that had multiple failures for the period 1960–2015. This can be represented by the distribution of  $\psi$ . Introducing a stronger factor for  $\psi$  in the forecasting method did show a shift in the ROC curve, with increasing TPR over FPR for higher threshold values but effectively no improvement in the prediction as AUC remains the same, because at lower threshold values TPR over FPR decreases. These findings indicate that the forecasting method could be improved in the future by adjusting the  $\psi$  variable, but this mainly improves the prediction for the observed locations with multiple collapses, and therefore consists of younger, less consolidated sediments. These multiple collapses occur at immobile tidal shoals that have a high and steep boundary, but are dynamic in vertical direction due to erosion and accretion, whereas horizontally dynamic shoals, due to channel migration, which is included in Equations (4)–(6), are not susceptible to collapse. We suggest including a vertical migration, i.e. aggradation, rate instead of the existing horizontal migration rate in Van den Ham *et al.* (2014), because  $\psi$  is only valid for liquefied flow slides, while shoal margin failures are dominated by breaching (Van den Berg *et al.*, 2017).

Analysis of the geometric shape of the erosion scar from the shoal margin collapses does not show a direct relation between the area size or volume with one of the variables, i.e.  $H_R$ ,  $\alpha_R$ ,  $\psi$  or  $Fr_{clay}$ . According to a multi-regression analysis, the collapsed size and volume are mostly affected by  $\alpha_R$ ,  $Fr_{clay}$  and  $\psi$ . The D-Flow Slide model (Deltares, 2017), based on the findings of Silvis and De Groot (1995), calculates the probability on a retrogression length of the erosion scar, which is a function of a number of geometric parameters before collapse and a volume balance between the material eroded from the scar and deposited at the toe. This method mainly predicts a larger retrogression length for a higher  $H_R$ , but according to our multi-regression analysis there is no relation between  $H_R$  and the geometric shape.

### Limitation and potential use of the forecasting method

The probability on bank collapses is a well-studied problem as many collapses either threatened or destroyed dikes and led to flooding. The additional data of shoal margin collapses from this study, combined with the historical database of (Wilderom, 1979), provides insights into the conditions under which collapses occur. Current bank assessments in the Netherlands are conducted on cross-sections representing a stretch of the bank (Deltares, 2017) and probabilities are tested for observed bank collapse locations (Stoutjesdijk *et al.*, 2012). This study proves that the forecasting method for determination of shoal margin collapses is also applicable to spatial data, and even for interpolated elevation data on a fixed Cartesian  $20 \times 20$  m grid, although the calculated



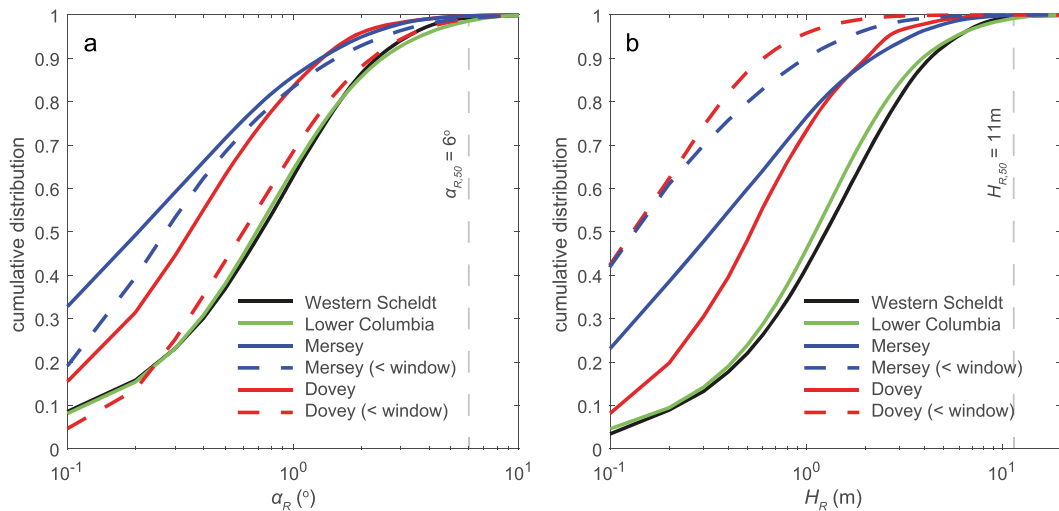


**Figure 12.** Cumulative distribution of  $\alpha_R$  and  $H_R$  for various estuaries. (a) The Western Scheldt and the Lower Columbia show steeper slopes than the Dovey and Mersey. (b) The Western Scheldt and the Lower Columbia also have higher slopes than the Dovey and Mersey. Note that with decreasing window size, because of the smaller estuary size of the Dovey and Mersey and assuming smaller collapses,  $\alpha_R$  is generally steeper whereas  $H_R$  decreases instead.

frequencies are evidently lower than observed and less than shown in earlier studies (Van den Ham *et al.*, 2014). We suspect that grid resolution smooths the steep slopes; nonetheless there remains a spatial variation in the probability that corresponds to locations that had collapses in the Western Scheldt.

There are limitations of the forecasting method, as we solely use bathymetry data of the Western Scheldt to determine locations that are susceptible to failure. We suspect that these collapses do occur in other estuaries, but have not been noted so far. In the Eastern Scheldt these collapses did occur, but after the Delta works the elevation of the tidal flats decreases (De Vet *et al.*, 2017) and so does the number of collapses. The forecasting method is designed to be generic and could be applied to other estuaries as well. Although shoal margin collapses are not reported for many other estuaries, analysis on bathymetry data of the Dovey and Mersey estuaries (see also Leuven *et al.*, 2018) shows that the relative slope angles and height are less than for the Western Scheldt (Figure 12). Bathymetry data of the Lower Columbia Estuary from 2009 to 2010 (Lower Columbia Estuary Partnership, 2010), however, show comparable slopes to the Western Scheldt (Figure 12) but no shoal margin collapses are reported in the literature. The steeper margins of the Lower Columbia Estuary consist of vegetated wetlands (Marcoe and Pilson, 2013), which strengthen the shoal margin against sudden collapses. The unvegetated tidal flats are lower, however, and therefore less susceptible to flow slides. The steeper and higher slopes in the Lower Columbia could, like the Western Scheldt, be associated with dredging activities, as a fairway is maintained towards Portland (Willingham, 1983; Cannon, 2015). Some of the lower unvegetated tidal flats are designated for the disposal of maintenance dredging material, e.g. at Rice Island and Miller Sands (Cannon, 2015). This could cause a flow side if the dumped material flows over the submerged slope, initiating an eroding turbulent density current, but would also lead to an increase in slope steepness and height.

The ROC curve indicates imperfect prediction, where the AUC is 0.7–0.8 rather than a preferred 0.9. Consequently, a large number of false positives are obtained. We attempted to improve the predictions by including some spatial variation in  $\psi$  and  $Fr_{\text{clay}}$ , which only slightly improved the prediction. On the other hand, we have not included any hydrodynamics in

our prediction, because there is no information available on the hydrodynamics during the failure, so we lack the precise trigger for a collapse. Liquefied flow slides are often observed in falling stage in rivers (Simon and Collinson, 2002) and falling tides (Christian *et al.*, 1998), because destabilization commonly occurs due to seepage of water out of the bank (Xie *et al.*, 2009), increasing the pore water pressure. The breaching process continues for hours, as observed in submarine canyons (Inman *et al.*, 1976), river banks (Coleman, 1969; Torrey, 1995), beach slopes (Beinssen *et al.*, 2014) and estuaries (Wilderom, 1961, 1964, 1968, 1973; Silvis and De Groot, 1995; Van den Berg *et al.*, 2002), and require only a minor trigger (Van Rhee and Bezuijen, 1998), which explains the rather erratic nature of these events in time and space.

Morphodynamic models show a tendency to overdeepen channels with the current transverse slope predictors (Van der Wegen and Roelvink, 2012). Overestimating the transverse slope effect in the morphodynamic model, and thus more downslope sediment transport, may be necessary to flatten the morphology and compensate for subgrid bank erosion processes, which usually does not occur in the numerical models (Grenfell, 2012; Schuurman *et al.*, 2013; Van Dijk *et al.*, 2014). Baar *et al.* (2018), however, concluded that overdeepening is not a direct result of the current transverse bed slope predictors. We propose to implement the forecasting method in a numerical morphodynamic model such as Braat *et al.* (2017) to oppose the transverse bed slope effect that steepens the shoal margin slope. Including the process of shoal margin collapses into a morphodynamic model might reduce the tendency to overdeepen the channels without having to overestimate the transverse bed slope predictor. The first step towards implementation of shoal margin collapses could be to replace the existing (overly simplistic) bank erosion forecasting method with the modified forecasting method, which collapses all slopes above a critical probability to a post-event slope while conserving mass. The geometric shape of the erosion scar, i.e. the semi-axis  $abc$ , could be calculated for a given eccentricity, shoal margin collapse size and the volume for a geometric shape of 1/3 ellipsoid as follows:

$$a = \frac{\sqrt{A_{\text{collapse}}}}{\sqrt{\pi} \cdot \sqrt[4]{1 - \varepsilon^2}} \quad (10)$$

$$b = \sqrt{a^2 - \varepsilon^2 \cdot a^2} \quad (11)$$

$$c = \frac{3 \cdot V_{\text{collapse}}}{\frac{4}{3} \pi ab} \quad (12)$$

where  $\varepsilon$  varies between 0.75 and 1. There is no direct relation between the variables ( $H_R$  and  $\alpha_R$ ) and area size and volume. Therefore, we suggest that  $A_{\text{collapse}}$  and  $V_{\text{collapse}}$  should be randomly picked from the observed lognormal distribution, where for  $A_{\text{collapse}}$  the distribution is created with a  $\mu$  of 10.38 and a standard deviation  $\sigma$  of 0.88, and for  $V_{\text{collapse}}$  the distribution is created with a  $\mu$  of 11.59 and a standard deviation  $\sigma$  of 1.21, according to the 299 observed shoal margin collapses between 1959 and 2015.

A scientific application of our spatial shoal margin collapse forecasting method will be to test the role of perturbations of the deposited collapsed material in the main channel of tidal systems. In tidal systems perturbations likely propagate in both directions depending on channel ebb or flood dominance, but how far and how fast has not been studied. Connections to the rest of the network may also determine whether perturbations excite or dampen. Conceptually, the downstream water and sediment fluxes, flow momentum and curvature, and upstream-propagating backwater effects (Friedrichs and Aubrey, 1988) can be seen as propagation of a signal or perturbation. We hypothesize that such morphological perturbations within the system may dynamicize the presently underpredicted morphodynamics of estuaries as much as extreme events in the boundary conditions.

## Conclusions

We studied the dimensions, geometry and probability of shoal margin collapses in the Western Scheldt for the period 1959–2015 and determined characteristic locations on various tidal flats that are susceptible to shoal margin collapse. Shoal margin collapses occur at immobile tidal shoals that have a high and steep boundary, but are dynamic in vertical direction due to erosion and accretion, whereas horizontally dynamic shoals, due to channel migration, are not susceptible to collapse.

We tested a modified algorithm that, for the first time, is applied to bathymetry data to assess the probability of shoal margin collapses; this showed that the probability of shoal margin collapses spatially varies but the frequency of collapses is, on average, lower than observed. The spatial variation in the probability is, however, sufficient to predict shoal margin collapse locations according to the ROC curve. In future studies we will be able to implement the forecasting method and apply a realistic geometric shape of shoal margin collapse, and study the role of shoal margin collapses on the long-term development of estuaries. Nevertheless, the forecasting method could be further improved for locations with multiple shoal margin collapses by including a vertical accretion rate factor rather than the lateral migration rate that was included in previous studies.

Specifically, our results can be summarized as follows:

- Tidal shoals are mainly found where the estuary width exceeds the ideal trumpet shape.
- Shoal margin collapses occur at locations where the summed width of shoals exceeds the excess width. When the channel banks are fixed or protected, these shoals are laterally inactive and shoal margin collapses occur as these shoals are vertical dynamic, i.e. steepening of the slope followed by flow slides.

- Shoal margin collapses cover on average an area of 34 000 m<sup>2</sup> and a volume of 100 000 m<sup>3</sup>, with volumes up to more than 10<sup>6</sup> m<sup>3</sup>, and contribute about 2% of the total erosion in the Western Scheldt.
- The geometric shape of the shoal margin collapse can be simplified by 1/3 of an ellipsoid for the purposes of modeling.
- Slope height and angle are good indicators to predict the locations for shoal margin collapses in the Western Scheldt.
- The forecasting method is rewritten in a form that would be applicable to a numerical model study for testing the role of natural perturbations on channel–shoal morphodynamics.
- The forecasting method was only tested on Western Scheldt data but provides indications where these collapses may be recognized in sandy estuaries worldwide.

*Acknowledgements*—This project was supported by the Netherlands Organisation for Scientific Research (NWO, grant STW-Vici-016.140.316/13710 to MK for WvD and JL). We gratefully acknowledge Marco Schrijver (Rijkswaterstaat Zee en Delta) and Marcel Taal (Deltares) for insightful discussions. We thank Rijkswaterstaat for providing the bathymetry data of the Western Scheldt. Constructive and positive reviews by two anonymous reviewers helped to clarify and strengthen the manuscript. To obtain the data from Rijkswaterstaat used in this paper, please contact the authors or visit <https://data.overheid.nl>.

## References

- Baar AW, De Smit J, Uijttewaal WSJ, Kleinhans MG. 2018. Sediment transport of fine sand to fine gravel on transverse bed slopes in rotating annular flume experiments. *Water Resources Research* **54**(1): 19–45.
- Beinssen K, Mastbergen DR. 2017. Flow slides: understanding their geo-mechanical mechanisms, the threats they pose and how these can be managed. In *13th Hydraulics in Water Engineering Conference (HIWE2017)*, Brady P, Felder S (eds), Sydney: Australia; 132–140.
- Beinssen K, Neil DT, Mastbergen DR. 2014. Field observations of retrogressive breach failure at the two tidal inlets in Queensland, Australia. *Australian Geomechanics* **49**(3): 55–64.
- Biot MA. 1941. General theory of three-dimensional consolidation. *Journal of Applied Physics* **12**(2): 155–164.
- Braat L, Van Kessel T, Leuven JRFW, Kleinhans MG. 2017. Effects of mud supply on large-scale estuary morphology and development over centuries to millennia. *Earth Surface Dynamics* **5**: 617–652.
- Cancino L, Neves R. 1999. Hydrodynamic and sediment suspension modelling in estuarine systems. *Journal of Marine Systems* **22**: 117–131.
- Cannon CM. 2015. *Landforms along the Lower Columbia River and the influence of humans*. Master's thesis, Portland State University.
- Christian HA, Monahan PA, Mosher DC. 1998. Initiation of underwater flowslides in a river and tide-dominated system: the Fraser river delta. In *International IAEG Conference*, Vol. 8, Balkema: Rotterdam; 3827–3832.
- Cleveringa J. Ontwikkeling mesoschaal Westerschelde: instandhouding vaarpassen Schelde Milieuvergunningen terugstorten baggerspecie [in Dutch], ARCADIS Amsterdam, 2013.
- Coleman JM. 1969. Brahmaputra River: channel processes and sedimentation. *Sedimentary Geology* **3**: 129–239.
- Dam G, Blik AJ, Labeur RJ, Ides S, Plancke Y. 2007. Long term process based morphological model of the Western Scheldt Estuary. In *Proceedings of the 5th IAHR Symposium on River, Coastal and Estuarine Morphodynamics*. Enschede, Netherlands; 1077–1084.
- De Groot MB, Mastbergen DR. 2006. Scour hole slope instability in sandy soil. In *Proceedings of the Third International Conference on Scour and Erosion*, CURNET: Gouda, Netherlands; 126–127.
- De Vet PLM, Van Prooijen BC, Wang ZB. 2017. The difference in morphological development between the intertidal flats of the Eastern and Western Scheldt. *Geomorphology* **281**: 31–42.

- De Vriend HJ, Wang ZB, Ysebaert T, Herman PMJ, Ding P. 2011. Ecomorphological problems in the Yangtze Estuary and the Western Scheldt. *Wetlands* **31**: 1033–1042.
- Deangeli C. 2007. The role of slope geometry on flowslide occurrence. *American Journal of Environmental Sciences* **3**(3): 93–97.
- Deltares. 2017. *Regeling veiligheid primaire waterkeringen 2017*. Bijlage III Sterkte en veiligheid [in Dutch]: Delft, Netherlands.
- Dunbar JB, Torrey VH, Wakeley LD. A case history of embankment failure: geological and geotechnical aspects of the Celotex levee failure, New Orleans, Louisiana, US Army Corps of Engineers Vicksburg, MS, 1999.
- Eke E, Parker G, Shimizu Y. 2014. Numerical modeling of erosional and depositional bank processes in migrating river bends with self-formed width: morphodynamics of bar push and bank pull. *Journal of Geophysical Research – Earth Surface* **119**: 1455–1483.
- Friedrichs CT, Aubrey DG. 1988. Nonlinear tidal distortion in shallow well mixed estuaries: a synthesis. *Estuarine, Coastal and Shelf Science* **26**(5): 521–545.
- Grenfell M. 2012. *Chute channels in large, sand-bed meandering rivers*, UK.
- Hayati H, Andrus RD. 2009. Updated liquefaction resistance correction factors for aged sands. *Journal of Geotechnical and Geoenvironmental Engineering* **135**(11): 1683–1692.
- IMDC. 2016. *Analyse historische plaatvallen oostelijk deel Westerschelde [in Dutch]*, Note. International Marine & Dredging Consultants, Antwerp, Belgium.
- Inman DL, Nordstrom CE, Flick RE. 1976. Currents in submarine canyon an air–sea–land interaction. *Annual Review of Fluid Mechanics* **8**: 275–310.
- Jentink R. Oprolging effecten flexibel storten, halfjaarrapportage Plaat van Walsorden tweede jaar 2015 [in Dutch], Rijkswaterstaat Centrale Informatievoorziening, Regio Zuid Middelburg, Netherlands, 2015.
- Jeuken MCJL. 2000. *On the morphologic behaviour of the tidal channels in the Westerschelde estuary*, Universiteit Utrecht.
- Jeuken MCJL, Wang ZB. 2010. Impact of dredging and dumping on the stability of ebb–flood channel systems. *Coastal Engineering* **57**: 553–566.
- Kleinhans MG. 2010. Sorting out river channel patterns. *Progress in Physical Geography* **34**: 287–326.
- Kleinhans MG, Schuurman F, Bakx W, Markies H. 2009. Meandering channel dynamics in highly cohesive sediment on an intertidal mud flat in the Westerschelde estuary, the Netherlands. *Geomorphology* **105**: 261–276.
- Laury RL. 1971. Stream bank failure and rotational slump: preservation and significance in the geologic record. *Geological Society of America Bulletin* **82**: 1251–1266.
- Leuven JRFW, De Haas T, Braat L, Kleinhans MG. 2018. Topographic forcing of tidal sand bar patterns for irregular estuary planforms. *Earth Surface Processes and Landforms* **43**: 172–186.
- Lowe DR. 1976. Subaqueous liquefied and fluidized sediment flows and their deposits. *Sedimentology* **23**(3): 285–308.
- Lower Columbia Estuary Partnership. 2010. Lower Columbia Digital Terrain Model. Available: <http://www.estuarypartnership.org/lower-columbia-digital-terrain-model> [7 April 2018].
- Marcoe K, Pilson S. Habitat change in the Lower Columbia River and Estuary, 1870–2011, Technical Report Technical report, Lower Columbia Estuary Partnership, EPA Washington, DC, 2013.
- Mastbergen DR. Oeverstabiliteit bij verdieping waterbodems: Rekenmodel HMBreach [in Dutch], Technical Report Technical report, Delft Cluster Netherlands, 2009.
- Mastbergen DR, Schrijvershof R. Sedimentatiepatronen Plaat van Walsorden na plaatval 22 juli 2014 [in Dutch], Technical Report Technical report, Deltares Delft, Netherlands, 2016.
- Mastbergen DR, Van den Berg JH. 2003. Breaching in fine sands and the generation of sustained turbidity currents in submarine canyons. *Sedimentology* **50**(4): 625–637.
- Mastbergen DR, Van den Ham GA, Cartigny M, Koelewijn A, De Kleine M, Hizett J, Azpiroz M, Vellinga A. 2016. Multiple flow slide experiment in the Westerschelde Estuary, The Netherlands. In *Submarine Mass Movements and their Consequences, 7th International Symposium: Advances in Natural and Technological Hazards Research*, Lamarche G, Mountjoy J, Bull S, Hubble T, Krastel S, Lane E, Micallef A, Moscardelli L, Mueller C, Pecher I, Woelz S (eds), Vol. 41, Springer: Wellington, New Zealand; 241–249.
- Olson SM, Stark TD. 2002. Liquefied strength ratio from liquefaction flow failure case histories. *Canadian Geotechnical Journal* **39**: 629–647.
- Savenije HH. 2015. Prediction in ungauged estuaries: an integrated theory. *Water Resources Research* **51**(4): 2464–2476.
- Schuurman F, Kleinhans MG, Marra WA. 2013. Physics-based modeling of large braided sand-bed rivers: bar pattern formation, dynamics, and sensitivity. *Journal of Geophysical Research – Earth Surface* **118**: 2509–2527.
- Shuttle DA, Jefferies MG. 1998. Dimensionless and unbiased CPT interpretation in sand. *International Journal for Numerical and Analytical Methods in Geomechanics* **22**: 351–391.
- Silvis F, De Groot MB. 1995. Flow slide in the Netherlands: experience and engineering practice. *Canadian Geotechnical Journal* **32**: 1086–1092.
- Simon A, Collinson AJC. 2002. Quantifying the mechanical and hydrologic effects of riparian vegetation on streambank stability. *Earth Surface Processes and Landforms* **27**(5): 527–546.
- Stoutjesdijk TP. Handboek zettingsvloeiing [in Dutch], Technical Report Technical report, Rijkswaterstaat, Dienst Weg- en Waterbouwkunde Delft, Netherlands, 1994.
- Stoutjesdijk TP, De Groot MB, Lindenberg J. 1998. Flow slide prediction method: influence of slope geometry. *Canadian Geotechnical Journal* **35**: 43–54.
- Stoutjesdijk T, Mastbergen DR, De Groot MB. Stormvloedkering Oosterschelde: ontwikkeling ontgrondingskuilen en stabiliteit bodembescherming, Deelrapportage Hellinginstabiliteit [in Dutch], Technical Report Technical report, Deltares Delft, Netherlands, 2012.
- TNO. 2016. DINO Database, GeoTOP version 1 release 3. Available: [https://www.dinoloket.nl/sites/www.dinoloket.nl/files/file/dinoloket\\_toelichtingmodellen\\_20160606\\_tno\\_2016\\_r10133\\_geotop\\_v1r3\\_english.pdf](https://www.dinoloket.nl/sites/www.dinoloket.nl/files/file/dinoloket_toelichtingmodellen_20160606_tno_2016_r10133_geotop_v1r3_english.pdf) [7 April 2018].
- Torrey VH. 1995. Flow slides in Mississippi riverbanks. In *River, Coastal and Shoreline Protection–Erosion Control: Using Riprap and Armourstone*, Thorne CR, Abt SR, Barendt BJ, Maynard ST, Pilarczyk KW (eds), Wiley: Chichester; 361–377.
- Van de Lageweg WI, Van Dijk WM, Baar AW, Rutten J, Kleinhans MG. 2014. Bank pull or bar push: what drives scroll-bar formation in meandering rivers? *Geology* **42**(4): 319–322.
- Van den Berg JH, Jeuken CJL, Van der Spek AJF. 1996. Hydraulic processes affecting the morphology and evolution of the Westerschelde estuary. In *Estuarine Shores: Evolution, Environments and Human Alterations*, Nordstrom KF, Roman CT (eds), Wiley: Chichester; 157–184.
- Van den Berg JH, Van Gelder A, Mastbergen DR. 2002. The importance of breaching as a mechanism of subaqueous slope failure in fine sand. *Sedimentology* **49**(1): 81–95.
- Van den Berg JH, Martinius AW, Houthuys R. 2017. Breaching-related turbidites in fluvial estuarine channels: examples from outcrop and core and implications to reservoir models. *Marine and Petroleum Geology* **82**: 178–205.
- Van den Ham GA, De Groot MB, Mastbergen DR. 2014. A semi-empirical method to assess flow-slide probability. In *Submarine Mass Movements and their Consequences. Advances in Natural and Technological Hazards Research*, Krastel S, Behrmann J-H, Volker D, Stipp M, Berndt C, Urgeles R, Chaytor J, Huhn K, Strasser M, Harbitz CB (eds), Vol. 37, Springer International: Cham, Switzerland; 213–223.
- Van der Wegen M, Roelvink JA. 2012. Reproduction of estuarine bathymetry by means of a process-based model: Western Scheldt case study, The Netherlands. *Geomorphology* **179**: 152–167.
- Van Dijk WM, Schuurman F, Van de Lageweg WI, Kleinhans MG. 2014. Bifurcation instability determines chute cutoff development in meandering gravel-bed rivers. *Geomorphology* **213**: 277–291.
- Van Dijk WM, Densmore AL, Sinha R, Singh A, Voller VR. 2016. Reduced-complexity probabilistic reconstruction of alluvial aquifer stratigraphy, and application to sedimentary fans in northwestern India. *Journal of Hydrology* **541**(B): 1241–1257.
- Van Duinen A, Bezuijen A, Van den Ham G, Hopman V. 2014. Field measurements to investigate submerged slope failures. In

- Submarine Mass Movements and Their Consequences*, Krastel S, Behrmann J-H, Volker D, Stipp M, Berndt C, Urgeles R, Chaytor J, Huhn K, Strasser M, Harbitz CB (eds), *Advances in Natural and Technological Hazards Research*, vol. 37, Springer International: Cham, Switzerland; 13–21.
- Van Rhee C, Bezuijen A. 1998. The breaching of sand investigated in large-scale model tests. In *Proceedings of the International Conference on Coastal Engineering*, Vol. 3, ASCE: Copenhagen; 2509–2519.
- Van Schaick S. 2015. *Morphological development after the July 2014 flow slide on the tidal flat of Walsoorden in the Western Scheldt*. Master's thesis, Delft University of Technology.
- Wang ZB, Winterwerp J. 2001. Impact of dredging and dumping on the stability of ebb–flood channel systems. In *Proceedings of the 2nd IAHR Symposium on River, Coastal and Estuarine Morphodynamics*, IAHR: Obihiro, Japan; 515–524.
- Wang ZB, Jeuken MCJL, Gerritsen H, De Vriend HJ, Kornman BA. 2002. Morphology and asymmetry of the vertical tide in the Westerschelde estuary. *Continental Shelf Research* **22**: 2599–2609.
- Wiegmann N, Perluka R, Oude Elberink S, Vogelzang J. *Vaklodingen: de inwintechnieken en hun combinaties: vergelijking tussen verschillende inwintechnieken en de combinaties ervan* [in Dutch], Technical Report Technical report, Adviesdienst Geo-Informatica en ICT (AGI) Delft, Netherlands, 2005.
- Wilderom MH. 1961. *Tussen afsluitdammen en deltadijken, I Noord-Beveland* [in Dutch]. Rijkswaterstaat: Utrecht, Netherlands.
- Wilderom MH. 1964. *Tussen afsluitdammen en deltadijken, II Noord-Zeeland* [in Dutch], Rijkswaterstaat: Utrecht, Netherlands.
- Wilderom MH. *Tussen afsluitdammen en deltadijken, III Midden-Zeeland* [in Dutch], Rijkswaterstaat Utrecht, Netherlands, 1968.
- Wilderom MH. 1972. *Plaatvallen* [in dutch]. *OTAR* **57**(7): 288–305.
- Wilderom MH. 1973. *Tussen afsluitdammen en deltadijken, IV Zeeuwsch Vlaanderen* [in Dutch], Rijkswaterstaat: Utrecht, Netherlands.
- Wilderom MH. Resultaten van het vooroveronderzoek langs de Zeeuwse stromen [in Dutch], Rijkswaterstaat Utrecht, Netherlands, 1979.
- Willingham WF. *Army engineers and the development of Oregon: A history of the Portland District*, Technical Report, US Army Corps of Engineers, 1983.
- Xie L, Lei H, Yu Y, Sun X. 2009. Incipient motion of river-banks sediments with outflow seepage. *Journal of Hydraulic Engineering* **135**(3): 228–233. [https://doi.org/10.1061/\(ASCE\)0733-9429\(2009\)135:3\(228\)](https://doi.org/10.1061/(ASCE)0733-9429(2009)135:3(228)).
- You Y, Flemings P, Mohrig D. 2014. Mechanics of dual-mode dilatative failure in subaqueous sediment deposits. *Earth and Planetary Science Letters* **397**: 10–18.